



**HAL**  
open science

# Provenance constraints on the Cretaceous-Paleocene erosional history of the Guiana Shield as determined from the geochemistry of clay-size fraction of sediments from the Arapaima-1 well (Guyana-Suriname basin)

Martin Roddaz, Guillaume Dera, Yannick Murlot, G r me Calv s,  
Jung-Hyun Kim, Anne-Claire Chaboureau, St phanie Mounic, Fran ois  
Raisson

## ► To cite this version:

Martin Roddaz, Guillaume Dera, Yannick Murlot, G r me Calv s, Jung-Hyun Kim, et al.. Provenance constraints on the Cretaceous-Paleocene erosional history of the Guiana Shield as determined from the geochemistry of clay-size fraction of sediments from the Arapaima-1 well (Guyana-Suriname basin). *Marine Geology*, 2021, 434, pp.106433. 10.1016/j.margeo.2021.106433 . hal-03245370

**HAL Id: hal-03245370**

<https://ut3-toulouseinp.hal.science/hal-03245370>

Submitted on 9 Mar 2023

**HAL** is a multi-disciplinary open access archive for the deposit and dissemination of scientific research documents, whether they are published or not. The documents may come from teaching and research institutions in France or abroad, or from public or private research centers.

L'archive ouverte pluridisciplinaire **HAL**, est destin e au d p t et   la diffusion de documents scientifiques de niveau recherche, publi s ou non,  manant des  tablissements d'enseignement et de recherche fran ais ou  trangers, des laboratoires publics ou priv s.



Distributed under a Creative Commons Attribution - NonCommercial 4.0 International License

1 **Provenance constraints on the Cretaceous-Paleocene erosional history of the Guiana Shield as**  
2 **determined from the geochemistry of clay-size fraction of sediments from the Arapaima-1 well**  
3 **(Guyana-Suriname basin)**

4  
5 Martin Roddaz<sup>1\*</sup>, Guillaume Dera<sup>1</sup>, Yannick Mourlot<sup>1</sup>, G r me Calv s<sup>1</sup>, Jung-Hyun Kim<sup>2</sup>,  
6 Anne-Claire Chaboureau<sup>3</sup>, St phanie Mounic<sup>1</sup> and Fran ois Raison<sup>3</sup>

7 <sup>1</sup> G osciences-Environnement Toulouse, Universit  de Toulouse; UPS (SVT-OMP); CNRS;  
8 IRD; 14 Avenue  douard Belin, F-31400 Toulouse, France

9 <sup>2</sup> Korea Polar Research Institute (KOPRI), 26 Songdomirae-ro, Yeonsu-gu, Incheon 21990,  
10 South Korea

11 <sup>3</sup> Total E&P, CSTJF Avenue Larribau, F-64018, Pau Cedex, France

12 \*Corresponding author: Martin Roddaz (martin.roddaz@get.omp.eu)

13

14 **Abstract**

15         Recent studies have emphasized the role of the Equatorial Atlantic Ocean opening on the  
16 drainage reorganization and erosion of the West African and northeastern Brazilian cratons  
17 during the Cretaceous. However, such studies are lacking regarding the Guiana Shield. To fill  
18 this gap, we determined the provenance of sediments deposited in the Suriname-Guyana basin  
19 during the Cretaceous-Paleocene based on the total organic carbon (TOC) content,  $\delta^{13}\text{C}_{\text{TOC}}$ ,  
20 major and trace element concentrations, and Sr-Nd isotopic data of nineteen clay-size fraction  
21 samples from one industrial well (Arapaima-1). Overall, the absence of correlation between the  
22 TOC content,  $\delta^{13}\text{C}_{\text{TOC}}$  and provenance proxies as well as the lack of Ce anomaly indicate that  
23 marine authigenesis, reducing conditions, and weathering have not markedly affected the trace  
24 element ratios (Eu/Eu\*, Cr/Th, Th/Sc) and Sr-Nd isotopic compositions used as provenance  
25 proxies. Three samples (Early Cretaceous, Cenomanian and Late Campanian) have radiogenic  
26  $\epsilon_{\text{Nd}(0)}$  values  $>-2.2$ . The Early Cretaceous sample may have been sourced by Precambrian or  
27 Mesozoic mafic rocks of the Guiana Shield or contemporaneous basic volcanic rocks. The  
28 Cenomanian sample is likely to have been sourced by basic volcanic rocks of the Caribbean  
29 Large Igneous Province or the Takutu rift whereas the Late Campanian sample may have  
30 recorded more acid volcanism in the Takutu Rift. The other samples have an overall Guiana  
31 cratonic provenance with variable contributions of the Paleoproterozoic and Mesoproterozoic  
32 terranes and Jurassic or Precambrian mafic dykes. Increases in  $^{87}\text{Sr}/^{86}\text{Sr}$  ratios and trace element  
33 ratios characteristic of more differentiated sources suggest an increasing contribution from the  
34 inner part of the Guiana Shield after the Coniacian. Because of the possible presence of active  
35 volcanism during the deposition of analyzed samples, post rift mantle upwelling under the

36 equatorial margin is the favored mechanism to explain the increasing erosion of the Guiana  
37 Shield inner parts.

38 **Keywords:** Provenance, Cretaceous, Guiana Shield, Guyana-Suriname Basin,

39

## 40 **1. Introduction**

41           The structure and geodynamic evolution of transform continental margins have recently  
42 received a lot of attention (i.e. Basile, 2015; Mercier de Lépinay et al., 2016; Nemčok et al.,  
43 2016). In particular, the conjugate West African, Suriname, Guyana, French Guiana and  
44 Brazilian equatorial margins are among the best examples (Basile et al., 2005; Emery et al.,  
45 1975; Mascle and Blarez, 1987; Mercier de Lépinay et al., 2016). Whereas the kinematics  
46 evolution of the Equatorial Atlantic Ocean and its margins is well constrained in time and space  
47 (Heine et al., 2013; Moulin et al., 2010), less attention has been paid to the erosional history of  
48 adjacent source areas (i.e., West African and Guiana and Brazilian cratons or Phanerozoic  
49 basins). Noticeable exceptions regarding the African margin is the provenance study of Mourlot  
50 et al. (2018a) which emphasized that the West African Craton (WAC) may be viewed as a  
51 dynamic area during the Cretaceous opening of the Equatorial Atlantic Ocean. Using the Nd  
52 isotopic composition of marine sedimentary rocks sampled offshore along the African margin,  
53 these authors have highlighted that the erosion the WAC evolved from its outer parts in the  
54 Albian–Middle Cenomanian interval to its inner parts in the Campanian–Maastrichtian (Mourlot  
55 et al., 2018a).

56           Like other Atlantic passive margins, the Brazilian and Guyana-Suriname margins are  
57 bordered by elevated low relief inland plateaus separated from a a higher relief coastal plain by  
58 one or more steep escarpments (Cogné et al., 2012; Gallagher et al., 1994; Gallagher and Brown,  
59 1999; Hiruma et al., 2010; Japsen et al., 2012; Jelinek et al., 2014; Tello Saenz et al., 2003). The  
60 presence of a Late Cretaceous “peneplanation surface” in the inner part of the Guiana Shield  
61 cropping out at elevation > 900 m asl is ascribed to Campanian erosion that may have affected  
62 this part of the Guiana Shield (Sapin et al., 2016). In northeastern Brazil, various

63 thermochronological and geomorphological studies have presented evidences of Late Cretaceous  
64 uplift (Harman et al., 1998; Morais Neto et al., 2009; Peulvast and Bétard, 2015; Potter, 1997).  
65 However, all these studies are based on mapping or sampling of isolated Cretaceous outcrops  
66 and this may question the representativeness of these studies at basin scale. To date there is no  
67 provenance study dealing with the Cretaceous erosional history of the Guiana Shield.

68         Determining the provenance of well dated deep-sea sediments deposited in marginal  
69 basins may be particularly useful to provide constraint on the erosional history of cratons (Clift  
70 and Blusztajn, 2005; Mourlot et al., 2018a). Many tools exist to determine the provenance of  
71 sedimentary rocks including sandstone petrography, clay mineralogy, heavy mineral analyses,  
72 geochronological dating on accessory minerals, major and trace element geochemistry and Sr-  
73 Sm-Nd isotopic compositions of bulk sedimentary rocks (see for instance Basu et al., 1990;  
74 Caracciolo, 2020; Cullers, 2000; Dickinson, 1985; Dickinson and Suczek, 1979; Garzanti, 2016,  
75 2019; Garzanti and Andò, 2019; McLennan et al., 1993a; Weltje, 2012 and references therein).  
76 All of these tools are subjected to biases related to source-rock mineral fertility (see for instance  
77 Chew et al., 2020; Dickinson, 2008; Malusà et al., 2016, 2013), pre and post depositional  
78 processes including weathering, grain-size sorting and diagenesis (see for instance (Bouchez et  
79 al., 2011; Fedo et al., 1995; Garzanti et al., 2008, 2009, 2014; Lawrence et al., 2011; McLennan  
80 et al., 1993a; Moquet et al., 2020; Nesbitt et al., 1996; Roddaz et al., 2006, 2014; Rousseau et al.,  
81 2019; Viers et al., 2008) and analytical procedures (Andersen et al., 2019; Chew et al., 2020;  
82 Malusà et al., 2013; Vermeesch, 2018, 2004). In addition, the low amount of material available  
83 for well or core sample makes geochronological dating methods (especially U-Pb dating on  
84 zircon) difficult to use. Trace elements ratios (i.e. Th/Sc, Cr/Th, Eu/Eu\*) as well as Sr-Nd  
85 isotopic composition of clay size sediments may be preferred to establish a complete integration

86 of drainage pathways from the most distant cratonic areas to oceanic basins (Patchett et al.,  
87 1999) because they are not biased by grain-size sorting (e.g. Cullers, 2000; McLennan et al.,  
88 1993) and require a lower amount of bulk sediment (~3 g, Bayon et al., 2002) These  
89 geochemical approaches have been recently used to determine the source of the Late Eocene to  
90 Quaternary sediments deposited in the Mozambique Channel (Roddaz et al., 2020) or to  
91 reconstruct the Cretaceous erosional history of the WAC (Mourlot et al., 2018). Furthermore, the  
92 Nd isotopic composition of past sediments deposited in ocean margins can provide constraints  
93 for determining the influence of continental Nd inputs released from river-borne lithogenic  
94 sediments deposited at ocean margins on Nd isotopic composition of past oceans. Indeed, Rare  
95 Earth Elements (REE) release from lithogenic sediments in river discharge may ultimately  
96 dominate all other REE inputs to the oceans (Jeandel et al., 2007; Jeandel and Oelkers, 2015;  
97 Rousseau et al., 2015). Such constraints are crucial for all oceanic circulation reconstruction  
98 based on the Nd composition of past oceanic masses (e.g. (Dera et al., 2015; Donnadiou et al.,  
99 2016; Mourlot et al., 2018b). Currently, the only Nd isotopic data available for the Cretaceous  
100 sediments of the Guyana and Brazilian margins of the Equatorial Atlantic Ocean are those from  
101 Martin et al. (2012). These data were obtained on fish teeth and sediments from the Demerara  
102 Rise (ODP Leg 207) which was a bathymetric high during the Cretaceous (e.g. Arthur and  
103 Natland, 1979. Loncke et al., 2019) and may have been potentially more influenced by oceanic  
104 currents than other parts of the equatorial margin basins.

105         The aim of this study is to determine the provenance of siliciclastic sediments deposited  
106 at the Suriname-Guyana basin during the Early Cretaceous-Paleocene based on TOC content,  
107  $\delta^{13}\text{C}_{\text{TOC}}$ , major and trace element concentrations and Sr-Nd isotopic data of nineteen clay-size  
108 fraction of sediment samples from one industrial well Arapaima-1 (AR-1, Fig. 1). Determining

109 the provenance of these sediments may help to bridge the gap between provenance studies  
110 regarding West African and Guiana cratons and may provide constraints on the erosional history  
111 of the Guiana craton.

## 112 **2. Geological setting and sedimentary sources**

### 113 2.1 Tectonic and geodynamic setting

114 The Guyana-Suriname basin is located along the passive margin of northeastern South  
115 America (Fig. 1). It includes the offshore of Guyana, Suriname and French Guiana. It is  
116 delimited by the Demerara Plateau to the east, the Barbados Ridge accretionary prism to the  
117 west, the Guiana shield to the south and the Demerara Abyssal plain to the north (Fig. 1). The  
118 tectonic evolution of the Guyana-Suriname basin can be divided into three main geodynamic  
119 periods linked to the opening of the Atlantic Ocean from the Early Jurassic (~200 Ma) to present  
120 (Yang and Escalona, 2011). The first geodynamic period is related to the Jurassic rifting between  
121 South America and North America. It was first initiated in the Central Atlantic region and  
122 resulted in east-west extension with a large component of dextral shearing in the Guyana-  
123 Suriname basin (Gouyet et al., 1994). This rifting period resulted in the formation of grabens in  
124 the present-day offshore region of the Guyana-Suriname basin and in the east-west-oriented  
125 Takutu graben separating the Guyana shield in two parts (Fig. 1). The thick (approximately 21  
126 km) volcanic basement of the Demerara Rise formed as a result of syn-rift-related volcanism  
127 linked to the Bahamas hot spot at the initial opening of the Central Atlantic (Basile et al., 2020;  
128 Reuber et al., 2016). This volcanism produced a marine substrate upon which the Late Jurassic-  
129 Early Cretaceous carbonate section of the Demerara rise developed (Basile et al., 2020; Reuber  
130 et al., 2016).

131           During the Early Cretaceous, Southern Africa and South America started to split off  
132 because of the counterclockwise rotation of Africa relative to South America (Mann et al., 1995;  
133 Pindell, 1991), resulting in two conjugate margins: the Guinea Rise on the African margin and  
134 the Demerara Rise on the South American margin. The drift stage of continental separation  
135 started to develop in the southernmost part of the South Atlantic Ocean at around 135 Ma (Late  
136 Valanginian–Early Hauterivian) (Hall et al., 2018) and then propagated northward toward the  
137 Equatorial Atlantic Ocean. This latter propagation of the South Atlantic rifting resulted in the  
138 formation of an erosional unconformity affecting the Guyana-Suriname basin and was  
139 responsible for the sedimentary hiatus between the upper Aptian and the lower Albian (Yang and  
140 Escalona, 2011). The pre-Albian section of the Demerara Rise was inverted and cut by a  
141 peneplanation surface with a strong angular unconformity prior to the Early Cretaceous opening  
142 of the Equatorial Atlantic seaway (Reuber et al., 2016).

143           The Equatorial Atlantic Ocean opened East of the Demerara Plateau during the Late  
144 Albian (see Moulin et al., 2010 and references therein). A kinematic change at 105 Ma (Albian)  
145 associated to the northward displacement of the triple junction between Africa, North America  
146 and South America plates (Müller and Smith, 1993) induced the formation of numerous E–W  
147 fracture zones North of the Demerara Plateau (Basile et al., 2013). Between the Albian and the  
148 Eocene, drifting between Africa and South America induced a general collapse of the unstable  
149 shelf edge and is responsible for the main extensional regime in the Guyana-Suriname basin  
150 (Yang and Escalona, 2011). This predominantly transcurrent setting may have favored the  
151 formation of a large pull-apart basin with a gentle thermal subsidence similar to the conjugated  
152 Guinean continental margin (Benkhelil et al., 1995).

153           2.2 Stratigraphy

154                   2.2.1 Stratigraphy of the Guyana-Suriname basin

155   The sedimentary infilling of the Guyana-Suriname basin may be divided into four stratigraphic  
156   sequences that overlay the Jurassic basement. These sequences are termed as follows: S1  
157   (Cretaceous), S2 (Paleogene), S3 (Early-Middle Miocene), S4 (Late Miocene to Pliocene) (Yang  
158   and Escalona, 2011). Details on the stratigraphy of the S1 sequence and associated references  
159   can be found in Yang and Escalona (2011). The S1 sequence starts with the Barremian basal  
160   clastic sandstones of the Stabroek Formation overlaid by the nonmarine siliciclastic deposits of  
161   the Potoco Formation. These formations are separated from the Albian to Turonian shelf marine  
162   platform deposits belonging to the Canje Formation by a Late Aptian–Early Albian(?) regional  
163   unconformity. The Canje Formation is composed of black shales with average total organic  
164   contents (TOC) between 4 and 7%, and reaching 29% in the Demerara Rise in the DSDP Site  
165   1259 (Meyers et al., 2006). These formations are then overlaid by the New Amsterdam  
166   Formation, a siliciclastic interval interpreted as a coastal environment with sand and lagoonal  
167   deposits (Lawrence and Coster, 1985). This formation corresponds to reservoirs in the  
168   Arapaima-1 well in offshore Guyana (Yang and Escalona, 2011). The top of the Mesozoic is  
169   marked by an erosional unconformity overlaid by Paleocene to Eocene carbonate shelf deposits  
170   of the George Town Formation (Yang and Escalona, 2011).

171                   2.2.2 Stratigraphy of the Arapaima-1 well

172           The stratigraphy and sedimentology of Cretaceous sequences of the Arapaima-1 well  
173   were reinterpreted by the TOTAL department of stratigraphy (Mourlot, 2018) and are presented  
174   in Fig. 2. The Early Cretaceous (pre-Aptian) is characterized by medium to coarse grained

175 sandstones with common shale and limestone intervals deposited in inner to outer shelf  
176 paleoenvironments. These clastic deposits are then separated from Late Albian shelf limestones  
177 by an erosional unconformity. These Late Albian shelf limestone are then overlaid by the first  
178 sequence of green to grey shales slightly enriched in TOC (1% wt) associated with a lowering of  
179 the sedimentation rate (Mourlot, 2018). This sequence is gradually overlain by Cenomanian  
180 deposits characterized by alternation of shales and sandstones. A two fold increase in  
181 sedimentation rate is noted for the Cenomanian clastic deposits when compared with older Early  
182 Cretaceous sediments (Mourlot, 2018). This Cenomanian clastic sequence is then followed by  
183 Cenomanian middle to outer shelf limestone deposits. The uppermost Cenomanian to Coniacian  
184 deposits consist in dark-grey to brown shales interbedded with siltstone and very fine sandstone  
185 and are characterized by an increase of organic-content (from 2% wt up to 4% wt, Fig. 2). This  
186 sequence can be correlated with the Canje Formation which is also composed of organic rich  
187 shales with average TOC between 4 and 7%. During the same period, the Demerara plateau also  
188 record an enrichment in Total Organic Carbon, with the TOC concentration reaching up to 29%  
189 at DSDP Site 1259 (Meyers et al., 2006). The Santonian to Paleocene sediments are  
190 characterized by alternation between medium to coarse sandstones and mainly non organic rich  
191 shales. The sedimentation rate is much higher during the Santonian, respectively six fold and  
192 three fold than the Early Cretaceous–Late Albian and Cenomanian–Coniacian intervals  
193 (Mourlot, 2018).

### 194 2.3. Sedimentary sources

195 The potential sources of the studied sediments include the Guiana Shield, the proto  
196 Andes, and the Caribbean Large Igneous Province magmatic rocks. Additionally, Aptian-Albian  
197 volcanism encountered on the Guinea Plateau (Olyphant et al., 2017) may be a potential source.

198 The Albian volcanoclastic units were dated at *ca* 106 Ma (Olyphant et al., 2017) and related to  
199 the silica under-saturated alkaline-nepheline-syenite suite of the Los Archipelago ring structure  
200 dated at  $ca\ 104.3 \pm 1.7$  Ma and located off the south-western shore of Conakry, Guinea (Moreau  
201 et al., 1996) . The Guiana Shield is mainly composed by Paleoproterozoic magmatic and  
202 metamorphic rocks accreted to two Archean nuclei during the main or late phase of the Trans-  
203 Amazonian orogeny (i.e., the Imataca block to the northwest and the Amapá block to the  
204 southeast; AAIG in Fig.3) (Delor et al. 2003; da Rosa-Costa et al., 2006; Gaudette et al., 1996,  
205 1978; McReath and Faraco, 2005; Vanderhaeghe et al., 1998). Based on geochronological and  
206 structural data, the Guiana shield may be divided into six main provinces decreasing in age  
207 southwestward from 2.5 to 1.2 Ga: Amazônia Central, Maroni-Itacaiúnas, Tapajós-Ventuari, Rio  
208 Negro-Juruena, Rondônia-San Ignacio, and Sunsás (Santos et al., 2000; Teixeira et al., 1989;  
209 Cordani et al. 2000). From a lithological point of view, the northernmost part of the shield is  
210 occupied by an extended greenstone belt (GB) amalgamated with Paleoproterozoic granitoids,  
211 gneiss, and felsic (meta)volcanic series (PGGF) (Barreto et al., 2013; Gruau et al., 1985), and  
212 bounded to the south by a high-grade granulite belt (PHGB) (Klaver et al., 2015; de Roever et al.  
213 2003). Overall, the rest of the shield is dominated by younger Paleoproterozoic PGGF marked by  
214 intrusions of Mesoproterozoic granite plutons (MG) in the Rio Negro province (Tassinari 1981;  
215 Sato 1998; Heinonen et al., 2012). Paleoproterozoic sediments related to the erosion of the  
216 Trans-Amazonian orogen are also present in the northwest part of the shield and consist in 3000  
217 m thick alternations of sandstones, conglomerates and pyroclastic rocks (PRS) belonging to the  
218 Roraima Formation (Priem et al., 1973). All the units cited above are intruded by sparse  
219 Paleoproterozoic mafic intrusions (PMI) (i.e., Avanavero dolerites, (Hebeda et al., 1973; Reis et

220 al., 2013) as well as Jurassic mafic dykes and sills (JMD) related to the Central Atlantic  
221 Magmatic Province (CAMP) activity at 200 Ma (De Min et al. 2003; Deckart et al., 2005).

222 As mentioned above, a rifting affected the Guiana shield from the Jurassic to Cretaceous,  
223 resulting in the formation of grabens stretching from SW Guyana to northern Brazil and  
224 constituting the Takutu basin. Upstream of the paleo-Berbice delta (Erlich and Keens-Dumas  
225 2007), this narrow intracratonic basin is especially important as it could represent the main  
226 pathway of the Berbice paleodrainage network during the Cretaceous (Figs. 1 and 3) (Lujan and  
227 Armbruster, 2011). The infilling of the basin consists first of the 900-1700 m thick tholeiitic  
228 basalts of the poorly dated Apoteri volcanic Formation (Crawford et al., 1985). A Jurassic age is  
229 commonly ascribed to these basaltic rocks (Berrangé and Dearnley, 1975; Crawford et al., 1985;  
230 Yang and Escalona, 2011), in association to the volcanic events of the Central Atlantic Magmatic  
231 Province (CAMP) with peak activity at 200 Ma (Marzoli et al., 1999). However, two K/Ar  
232 radiometric dating on basaltic lava flows yield Early Cretaceous ages at  $114 \pm 3$  Ma and  $116 \pm 4$   
233 Ma (Berrangé and Dearnley, 1975) so that the Apoteri volcanic Formation might be younger  
234 than previously thought. Overlying the Apoteri volcanic Formation are the poorly dated shales  
235 and halites of the Manari and Pirara formations followed by the 1600 cm to 3500 m thick  
236 Jurassic to Cretaceous shales, sandstone, siltstones, and micritic limestones of the Takutu  
237 Formation (Crawford et al., 1985). This formation developed in fluvial and coastal settings.  
238 Pyroclastic flows, up to 87% in SiO<sub>2</sub> content, are recorded in the upper part of the Takutu  
239 Formation (Crawford et al., 1985).

240 All the geological units of the Guiana Shield defined above present different ages and  
241 lithologies (mafic vs. felsic) making them suitable to distinguish in term of major and trace  
242 elemental compositions but also  $^{87}\text{Sr}/^{86}\text{Sr}$  and  $\epsilon\text{Nd}(0)$  values. To better characterize the sources

243 of studied Cretaceous-Paleocene sediments, we compiled 568 published Sr and Nd isotope  
244 values measured on magmatic and metamorphic rocks representative of six characteristic end-  
245 members of the Guiana shield (Table 1 and supporting information Table S1 for details and  
246 references). By increasing  $\epsilon\text{Nd}_{(0)}$  value, these latter include the Archean granitoids (AAIG) with  
247 median  $\epsilon\text{Nd}_{(0)}$  and  $^{87}\text{Sr}/^{86}\text{Sr}$  values at -31.4 (standard deviation (S.D.): 9.3, Table 1) and 0.79509  
248 (S.D.: 0.335623, Table 1), the Paleoproterozoic granitoids and felsic series (PGGF) at -23.4  
249 (S.D.: 8.0, Table 1) and 0.77395 (S.D.: 0.4638016, Table 1) the Paleoproterozoic high-grade belt  
250 (PHGB) at -21.2 (S.D.: 6.2, Table 1) and 0.72025 (S.D.: 0.1571444, Table 1), the  
251 Mesoproterozoic granitoids (MG) at -18.5 (S.D.: 2.1, Table 1) and 0.77460 (S.D.: 0.05247612,  
252 Table 1), the Paleoproterozoic mafic intrusions and greenstone belt (PMI-GB) at -8.9 (S.D.: 7.1,  
253 Table 1) and 0.71051 (S.D.: 0.006878231, Table 1), and the Jurassic mafic dykes (JMD) at -0.2  
254 (S.D.: 3.1, Table 1) and 0.70647 (S.D.: 0.001692758, Table 1 and Fig. 3). For comparison, this  
255 database was completed by 47  $^{87}\text{Sr}/^{86}\text{Sr}$  and  $\epsilon\text{Nd}_{(0)}$  values of later Cretaceous to modern  
256 sediments deposited in the Demerara abyssal plain and Demerara Rise (Martin et al., 2012;  
257 Schulte et al., 2009; White et al., 1985), as well as 110 Sr-Nd isotopic compositions of  
258 suspended particulate matter and dissolved Sr transported by the main tropical rivers of the  
259 northeastern part of South America (i.e., Amazon, lower and upper Orinoco, Rio Negro, Maroni,  
260 Trombetas, Caroni) (Allègre et al., 1996; Goldstein et al., 1997; Palmer and Edmond, 1992;  
261 Rousseau et al., 2019; Santos et al., 2015).

### 262 **3. Materials and Methods**

#### 263 **3.1 Sampling**

264 Nineteen Early Cretaceous to Paleocene fine-grained sedimentary rocks were sampled  
265 from the Arapaima-1 exploration well (Fig. 1). These fine-grained sedimentary rocks were  
266 deposited in shallow marine mixed clastic and carbonates depositional environments. There is  
267 uncertainty regarding the limits between the Late Albian and the Cenomanian and between the  
268 Santonian and the Late Campanian in the well due to lack of biostratigraphic data. Otherwise, the  
269 time resolution of samples is at the sub-stage level (*i.e.*, ~2 to 3 Ma). These samples provide  
270 sufficient time resolution to identify long-term trends in sedimentary provenance.

### 271 3.2 Bulk organic geochemical analysis

272 The TOC content of sediments and its stable carbon isotopic compositions ( $\delta^{13}\text{C}_{\text{TOC}}$ )  
273 were analysed at the University of Hanyang (South Korea). Precisely weighed aliquots (0.5-16 g)  
274 of crushed and homogenized samples were decalcified by adding about 8 mL of 1M HCl. After  
275 shaking overnight (~12 h) to remove carbonates prior to analysis, the TOC content and  $\delta^{13}\text{C}_{\text{TOC}}$   
276 values were determined by EA-IRMS (elemental analyzer-isotope ratio mass spectrometry,  
277 EuroEA-Isoprime IRMS, GV instruments, UK). The TOC content and isotope values were  
278 calibrated against a standard (IAEA-CH-6, TOC = 42.1 %,  $\delta^{13}\text{C} = -10.44 \text{ ‰}$ ). The analyses were  
279 performed at least in duplicate. The TOC data are given in weight percentage (wt%) and the  
280  $\delta^{13}\text{C}_{\text{TOC}}$  values are reported in the standard delta notation relative to the Vienna Pee Dee  
281 Belemnite (VPDB) standard. The analytical precision (as standard deviation for repeated  
282 measurements of the internal standard IAEA-CH-6,  $n=18$ ) is 1.1 wt% for TOC and 0.2 ‰ for  
283  $\delta^{13}\text{C}_{\text{TOC}}$ .

## 284 3.3 Major and trace elements and Sr-Nd isotopes

### 285 *3.3.1 Sample preparation*

286 Each sample was finely crushed in an agate mortar. About 3 g of the crushed sediment  
287 were placed into 50 ml centrifuge tubes for sequential leaching to remove the non-terrigenous  
288 sedimentary components following the method of Bayon et al. (2002). Three different solutions  
289 composed of 5% acetic acid, 15% acetic acid and hydroxylamine hydrochloride (0.05 M) and  
290 hydrogen peroxide (H<sub>2</sub>O<sub>2</sub>, 5%) were then added to remove the carbonates, Fe-Mn oxides and  
291 organic carbon, respectively. After the removal of non-terrigenous components, the residual  
292 fractions were cleaned with ultrapure water (MQ-H<sub>2</sub>O, 18 MΩ). Clayey (<2 μm) and silty (2-63  
293 μm) fractions were then separated by centrifugation in two steps. First, 25 ml of MQ-H<sub>2</sub>O were  
294 added to the detrital residues in the tubes, shaken vigorously, and then centrifuged for 2 min at  
295 1000 rpm (133 g). The clay-rich supernatants were immediately transferred into new 50 ml  
296 centrifuge tubes. Another 25 ml of MQ-H<sub>2</sub>O was added to silt-rich detrital residues, mixed  
297 thoroughly again, centrifuged for 2.5 min at 800 rpm (85 g), and transferred into corresponding  
298 centrifuge tubes. Finally, clay-size fractions were collected after decantation (48 hours) and  
299 centrifugation at 3500 rpm (1630 g) (Bayon et al., 2015). These clay-size fractions were then  
300 analyzed for their major and trace element concentrations and their Sr-Nd isotopic compositions.

### 301 *3.3.2 Major and trace element analyses*

302 The major and trace element concentrations were measured at the Service d'Analyse des  
303 Roches et Minéraux (SARM, INSU facility, Vandoeuvre-Les-Nancy, France) by ICP-OES (Na,  
304 Mg, K, Ca, Sc, Ti, Mn, Fe, Al, Si and P) and ICP-MS (Rb, Cs, Ba, Sr, Th, U, Y, Zr, Nb, Hf, Cr,  
305 V, Co, Cu, Ni, Zn, La, Ce, Pr, Nd, Sm, Eu, Gd, Tb, Dy, Ho, Er, Tm, Yb, Lu and Ta ) after alkali

306 fusion. Analytical details are available on <http://helium.crpg.cnrs-nancy.fr/SARM/> and in  
307 Carignan et al. (2001). Uncertainty is lower than 5% for elements measured by ICP-OES, and  
308 lower than 10% for elements measured by ICP-MS (see supplementary material Table S2).

### 309 *3.3.3 Nd-Sr isotopes compositions*

310 The Nd-Sr isotopic compositions were measured at Géosciences Environnement Toulouse  
311 (GET) in France. About 100 mg of the leached detrital residue fractions were accurately weighed  
312 in cleaned Savillex PFA vials and then digested by several hot acid attacks. The analyzed  
313 fractions were firstly digested in hydrogen peroxide for 24 hours at ambient temperature, and  
314 then digested in HNO<sub>3</sub> for 24 hours at 80°C followed by HF-HNO<sub>3</sub> for 24 hours at 80°C, and,  
315 finally HCl+HNO<sub>3</sub> for 24 hours at 115°C. Blank tests were performed to estimate the level of  
316 contamination induced by the acid digestion, but it was found to be negligible. Aliquots  
317 containing about 1000 ng of Sr and Nd were loaded into the ion exchange columns. Strontium  
318 and Nd were separated using the Sr-SPEC, TRU-SPEC and LN-SPEC resins (Eichrom). The  
319 isotopic values of both elements were measured using a Finnigan Mat 261 thermal ionization  
320 mass spectrometer and a Triton Thermal Ionization Mass Spectrometer in dynamic mode during  
321 the same runs as performed for clay-size sediments of the DSDP 25 Site 242 analyzed in  
322 (Roddaz et al., 2020). During the Nd runs, a <sup>146</sup>Nd/<sup>144</sup>Nd ratio of 0.7219 was used to correct the  
323 signal for mass fractionation. For each sample, checks were made for the absence of Samarium  
324 (Sm). The accuracy of the measurements was estimated on the La Jolla standard. Repeated  
325 analyses of the La Jolla standard gave a <sup>143</sup>Nd/<sup>144</sup>Nd ratio of 0.511867 ± 0.000018 (2 S.D, n =  
326 12) in agreement with the recommended value of 0.511858 (Lugmair et al., 1983). During the Sr  
327 runs, <sup>86</sup>Sr/<sup>88</sup>Sr = 0.1194 was used to correct the <sup>86</sup>Sr signal for mass fractionation. The accuracy of the  
328 <sup>87</sup>Sr/<sup>86</sup>Sr measurements was checked against the NBS 987 standard (= 0.710240) Hodell et al.,

2007). Repeated analyses of the NBS 987 standard gave an  $^{87}\text{Sr}/^{86}\text{Sr}$  ratio of  $0.710231 \pm 0.000032$  (2SD,  $n=15$ ) in agreement with the recommended value of Hodell et al. (2007) therefore no instrumental bias needs to be taken into account. Total blanks (acid digestion plus column chemistry) for Nd and Sr were checked by ICP-MS and found to be negligible (<1 per mil) compared to the Nd and Sr amounts loaded onto the columns.

The measured  $^{143}\text{Nd}/^{144}\text{Nd}_{\text{sample}}$  ratios are expressed in epsilon notation as the fractional deviation in parts per  $10^4$  (units) from  $^{143}\text{Nd}/^{144}\text{Nd}$  value of the Chondritic Uniform Reservoir (CHUR). This notation is defined as:

$$\epsilon_{\text{Nd}(t)} = [({}^{143}\text{Nd}/{}^{144}\text{Nd})_{\text{sample}(t)} / ({}^{143}\text{Nd}/{}^{144}\text{Nd})_{\text{CHUR}(t)} - 1] \times 10^4$$

where  $t$  indicates the time at which  $\epsilon_{\text{Nd}}$  is calculated. Here, no time correction is applied ( $t = 0$ ) and the  $^{143}\text{Nd}/^{144}\text{Nd}_{\text{CHUR}(0)} = 0.512638$  (Jacobsen and Wasserburg, 1980).

340

## 341 **4. Results**

### 342 4.1 Organic geochemistry and $\delta^{13}\text{C}_{\text{TOC}}$ data

343 The TOC results for the Arapaima-1 well are variable with values ranging from 0.2 to 4.6  
344 wt% through the studied interval (Table 2). The Cenomanian to Santonian sedimentary rocks  
345 (AR1-11B to AR1-17B samples) appear to be more enriched in organic matter (TOC>2%)  
346 compared with other sedimentary rocks (Table 2 and Fig. 2). The  $\delta^{13}\text{C}_{\text{TOC}}$  of analyzed samples  
347 range between -28.4 (Cenomanian, samples AR1-11E and AR1-11F) and -25.0 (Early Turonian,  
348 sample AR1- 12A, Table 2). Compared with compilations of long-term Cretaceous trends in NW  
349 Tethyan and Pacific  $\delta^{13}\text{C}_{\text{bulk}}$  data (Bodin et al., 2015; Friedrich et al., 2012), our data show

350 similar sharp positive isotopic excursions in the Cenomanian (between samples AR1-9 and AR1-  
351 10, Table 2) and at the Cenomanian-Turonian boundary (samples AR1-11E and AR1-11F, Table  
352 2). However, the younger  $\delta^{13}\text{C}_{\text{TOC}}$  data do not fit the long-term Cretaceous evolution of  $\delta^{13}\text{C}_{\text{bulk}}$   
353 data recorded in the NW Tethyan and Pacific (Friedrich et al. 2012).

#### 354 4.2 Major elements, Large-Ion Lithophile Elements (LILE), High Field Strength 355 Elements (HFSE) and Trace Transition Elements (TTE)

356 Figure 4 shows the elemental concentrations of major elements, LILE, HFSE and TTE of  
357 samples normalized to the Post Archean Australian Shales (PAAS) concentration (Pourmand et  
358 al., 2012; Taylor and McLennan, 1985). As a whole, the elemental composition of the analyzed  
359 sample is rather uniform. They are all depleted in MnO, CaO, K<sub>2</sub>O, Rb, Cs, Sr, Th, Y, Zr, Nb, Hf  
360 et Co against PAAS (Table 3 and Fig. 4). With the exception of two Early Cretaceous samples  
361 (AR1-1 and AR1-7) and Santonian- Paleocene samples (AR1-21, AR1-23, AR1-24), they are  
362 enriched in Cr and V with respect to PAAS (Table 3 and Fig. 4). However, the analyzed samples  
363 are more contrasted regarding their concentrations in Na<sub>2</sub>O, P<sub>2</sub>O<sub>5</sub>, Ba and U against PAAS.  
364 Overall, Santonian-Paleocene sediments are less concentrated in major and trace elements when  
365 compared with older sediments. But, no apparent trend of major depletion or enrichment in  
366 elemental concentration is recorded with the age of sediments.

367 It is possible to assess the degree of source-area weathering and the paleoweathering  
368 conditions of ancient sediments using the Chemical Index of Alteration (CIA) (Fedo et al., 1995;  
369 Nesbitt and Young, 1982). This index measures the weathering intensity of feldspars relative to  
370 unaltered protoliths, and is defined as:  $\text{CIA} = [\text{Al}_2\text{O}_3 / (\text{Al}_2\text{O}_3 + \text{CaO}^* + \text{Na}_2\text{O} + \text{K}_2\text{O})] \times 100$  (in molar  
371 proportions), where CaO\* represents the CaO content in the silicate fraction. CIA values for  
372 unaltered plagioclase and K-feldspars typical of unaltered upper crustal rocks are approximately

373 equal to 50, whereas higher CIA values represent higher degrees of weathering. For comparison,  
374 the CIA value of the PAAS standard, which is representative of the upper continental crust  
375 composition, is equal to 67 (Taylor and McLennan, 1985).

376 Here, the CIA values of analyzed samples range from 61 to 89 and are therefore higher  
377 than those of the PAAS, except for one sample (AR1-7, CIA~61). Overall, and with the  
378 exception of the Coniacian sample AR1-17A (CIA~74), the Early Cretaceous samples (AR1-1,  
379 AR1-6, AR1-7) and Cenomanian samples (AR1-9 to AR1-11F) have lower CIA values (70-78,  
380 Table3) than younger Turonian to late Campanian samples (CIA  $\geq$  80, Table 3).

381 Early Cretaceous to Early Santonian samples have Cr/Th ratios higher than PAAS (37.9-  
382 10.2, Table 3) whereas younger samples have Cr/Th ratios lower than PAAS. Analyzed samples  
383 have Th/Sc ratios ranging between 0.27 and 1.12 (Table 3). With the exception of two  
384 Cenomanian samples (AR1-11E and AR1-11F), the Th/Sc ratios is increasing as the age of the  
385 samples is becoming younger (Table 3).

386

#### 387 4.3 Rare Earth Elements (REE)

388 To facilitate comparisons with sediments derived from basic or felsic sources (Cullers,  
389 2000) and the PAAS (Pourmand et al., 2012; Taylor and McLennan, 1985), the Eu anomaly is  
390 calculated with respect to chondrites:  $Eu/Eu^* = Eu_N / (Sm_N \times Gd_N)^{1/2}$  where  $N$  refers to the  
391 chondrite-normalized concentration value (Condie, 1993). The Cerium anomaly ( $\Omega_{Ce}$ )  
392 normalized to PAAS is calculated following (De Baar et al., 1985) :  $\Omega_{Ce} = 2 \times (Ce_{sample} / Ce_{PAAS})$   
393 /  $[(La_{sample} / La_{PAAS}) + (Pr_{sample} / Pr_{PAAS})]$ , where  $X_{sample}$  is the concentration of samples and  $X_{PAAS}$   
394 refers to the concentrations of the PAAS standard.

395           When normalized against PAAS, most of the analyzed samples have flat REE patterns  
396 and variable Eu anomalies (Fig. 5). The Santonian to Paleocene samples are more enriched in  
397 Light REE (LREE) and in Middle REE (MREE) than PAAS (Fig. 5). Three Cenomanian  
398 samples (AR1-11B, AR1-11D, AR1-11E) show enrichment in Heavy REE (HREE) against  
399 LREE and MREE (Fig. 5 and Table 3). The analyzed sample Ce anomalies display a narrow  
400 range of values (0.85-1.01) close to that of the PAAS standard (*i.e.*,  $\Omega_{Ce} = 1$ ). The analyzed  
401 values are systematically higher than those measured in authigenic smectites and seawater ( $\Omega_{Ce}$   
402  $< 0.50$ , De Baar et al., 1985) and they do not show any variation with stratigraphic position. The  
403 Eu/Eu\* ratios of the analyzed samples range between 1.26 and 0.67 and are higher compared to  
404 the PAAS standard (*i.e.*, Eu/Eu\* = 0.58). With the exception of one Cenomanian sample (AR1-  
405 10), there is an overall increase of the Eu anomaly (*i.e.* decrease of the Eu/Eu\* ratio) with the age  
406 of the sample (Figs 5 and 6 and Table 3).

#### 407           4.4 Sr-Nd isotopes

408           The  $^{87}\text{Sr}/^{86}\text{Sr}$  isotopic composition of the samples range from 0.714598 to 0.773011 while  
409 their  $\varepsilon_{\text{Nd}(0)}$  values range from -0.6 to -21.2 (Table 4). Median values for  $^{87}\text{Sr}/^{86}\text{Sr}$  isotopic  
410 compositions and  $\varepsilon_{\text{Nd}(0)}$  values are 0.736 and -18.8 respectively. There is no correlation between  
411 the Sr and Nd isotopic composition of analyzed samples (see Table S3 in supplementary dataset).  
412 Overall, the  $^{87}\text{Sr}/^{86}\text{Sr}$  ratios of Arapaima-1 well samples can be split into three groups. Samples  
413 AR1-1 (Early Cretaceous) to AR1-9 (Cenomanian) and Coniacian samples (AR1-17A and AR1-  
414 17B) have quite similar low radiogenic  $^{87}\text{Sr}/^{86}\text{Sr}$  ratios ranging between 0.721 and 0.733 (Table  
415 4). The other Cenomanian and the Turonian samples show strong variation in their  $^{87}\text{Sr}/^{86}\text{Sr}$   
416 ratios (0.715-0.761). And overall, if we except the Early Turonian sample (AR1-12A), the  
417 youngest late Santonian to Paleocene analyzed samples have the more radiogenic  $^{87}\text{Sr}/^{86}\text{Sr}$  ratios

418 of the analyzed samples (0.749-0.775, Table 4 and Fig. 6). Most of the analyzed samples have  
419 low radiogenic Nd isotope composition with  $\epsilon_{Nd(0)}$  values generally between -15.8 and -21.2  
420 (Table 4). Only three samples (Early Cretaceous AR1-1, Cenomanian AR1-11D and Late  
421 Campanian AR1-23) have high radiogenic signatures with  $\epsilon_{Nd(0)}$  values between -2.2 and -0.6  
422 (Table 4). Two samples (Cenomanian AR11E and Santonian? AR1-21) have intermediate Nd  
423 isotopic composition with  $\epsilon_{Nd(0)}$  values of -12.2 and -13.6 respectively (Table 4).

## 424 **5. Discussion**

425       5.1. Influence of weathering, authigenesis and anoxic conditions on provenance proxies  
426       The REE content, Eu anomalies, elemental ratios (Cr/Th and Th/Sc) and Sr-Nd isotopic  
427 compositions of sedimentary rocks may be used as robust tools for determining the provenance  
428 of marine sediments (McLennan et al., 1993), to the condition that they are not affected by  
429 weathering and syndepositional clay authigenesis. For instance, high Eu anomalies and Th/Sc  
430 and low Cr/Th are characteristic of felsic and more highly differentiated source rocks, whereas  
431 high Cr/Th and low Eu anomalies and Th/Sc suggest more mafic and less differentiated source  
432 rocks (Cullers, 2000; McLennan et al., 1993b). In general, these ratios as well as the REE  
433 content are not significantly affected by diagenesis or weathering (Cullers, 2000; Fedo et al.,  
434 1995; McLennan, 1989; McLennan et al., 1993a) The absence of any correlation (see Table S3 in  
435 supplementary dataset) of CIA and Al/Si with REE content, Eu/Eu\*, Cr/Th, Th/Sc,  $^{87}Sr/^{86}Sr$   
436 isotopic compositions and  $\epsilon_{Nd(0)}$  suggests that chemical weathering has not modified these  
437 provenance proxies. Regarding authigenesis effects, any influence from carbonates, Fe-Mn  
438 oxides or organic matter formed under marine conditions should have been removed by the  
439 sequential carbonate dissolution and leaching steps. In addition, there is no correlation between

440 TOC content and  $\delta^{13}\text{C}_{\text{TOC}}$  and provenance proxies (Eu/Eu\*, Cr/Th, Th/Sc,  $^{87}\text{Sr}/^{86}\text{Sr}$  isotopic  
441 compositions and  $\varepsilon_{\text{Nd}(0)}$ ) suggesting that enrichment and preservation of organic matter are not  
442 affecting these proxies. Moreover, the REE patterns of authigenic smectites formed in deep-  
443 water environments are characterized by LREE depletion, HREE enrichment and strong negative  
444 Ce anomalies ( $\Omega\text{Ce} < 0.50$ , De Baar et al., 1985) typical of seawater (Piper, 1974). Here, most of  
445 the analyzed samples have Ce anomalies higher than or equal to 0.85, with flat REE patterns  
446 against PAAS corresponding to the “shales” field in Fig. 7. Only three Cenomanian samples  
447 (AR1-11B, AR1-11D, AR1-11E) show enrichment in HREE over LREE and plot between the  
448 “shales” and “seawater” fields in Fig. 7. However, as they have low Ce anomalies against PAAS  
449 ( $\Omega\text{Ce}$  between 0.88 and 0.92), this suggests that, even if authigenic smectites might have been  
450 incorporated during early diagenetic processes, its proportion was much less than the detrital  
451 fraction. Finally, it is worth noting that diagenetic remobilization of Eu under reducing  
452 conditions might lead to the development of high positive Eu anomalies (MacRae et al., 1992).  
453 As anoxic to suboxic conditions are suggested from geochemical and sedimentological proxies  
454 onto the Demerara Rise (i.e., Ocean Drilling Program Leg 207 Site) in the Cenomanian-Turonian  
455 interval (Berrocoso et al., 2008; Hetzel et al., 2009), this process could explain the high Eu/Eu\*  
456 value (1.26) of the Cenomanian sample AR1-10 (Table 3 and Fig.6). However, anoxic conditions  
457 are also known to favor organic matter preservation and can be recorded by high TOC content  
458 (Algeo and Liu, 2020; Schlanger and Jenkyns, 1976), which is not the case for the AR1-10  
459 sample that has one of the lowest TOC content among the analyzed samples (i.e. 0.5%, Table 2).  
460 Rather, the samples with the highest TOC content (TOC>2%, Table 1) have lowest Eu/Eu\* ratios  
461 (0.72-0.88, Table 3) suggesting that diagenetic remobilization of Eu under reducing condition  
462 was negligible in our samples.

463

## 464 5.2. Provenance interpretation

465 Most of the  $\delta^{13}\text{C}_{\text{TOC}}$  values of analyzed samples have organic matter mainly of terrestrial origin  
466 because they have  $\delta^{13}\text{C}_{\text{TOC}}$  values within the range of C3 plant-derived organic matter (-29.3 to  
467 -25.5‰, mean ~27‰ (e.g. (Tyson, 1995) and depart from typical marine  $\delta^{13}\text{C}_{\text{TOC}}$  values (-18  
468 to -22‰ (e.g. (Meyers, 1997)). Hence, this suggests that the analyzed sedimentary rocks were  
469 mainly fed by continental detritus.

470 The potential sources of the studied sediments may include the rocks of the Guiana Shield,  
471 Northwestern Africa, the proto Andes and the Caribbean Large Igneous Province magmatic  
472 rocks. Here, we argue that a northwestern African provenance is unlikely because existence of  
473 bottom currents parallel to the northwestern African coast during the Cretaceous (Mourlot et al.,  
474 2018b) may have prevented the arrival of northwestern African detritus to the deep distal part of  
475 the Central Atlantic Ocean (Mourlot et al., 2018b). In addition, aerial transport from northwest  
476 Africa is also unlikely because  $\epsilon_{\text{Nd}(0)}$  values of our analyzed sedimentary rocks and those of the  
477 Demerara rise (Martin et al., 2010) show significant differences with those of contemporaneous  
478 sedimentary rocks deposited in the deep offshore Central Atlantic Ocean and northwestern  
479 African margin during the Albian-Maastrichtian times (Mourlot et al., 2018a). A proto-Andean  
480 provenance is not supported by the provenance of Cretaceous sedimentary rocks deposited in the  
481 Amazonian retroarc foreland basin because these sedimentary rocks are cratonic in provenance  
482 and were deposited by cratonic paleodrainage (Erlich et al., 2018; George et al., 2019; Hurtado et  
483 al., 2018; Louterbach et al., 2018) with very negative  $\epsilon_{\text{Nd}(0)}$  values (Hurtado et al., 2018;  
484 Louterbach et al., 2018) originated from the Central part of the Amazon Shield (Hurtado et al.,  
485 2018).

486 When plotted on a  $^{87}\text{Sr}/^{86}\text{Sr}$  vs.  $\epsilon_{\text{Nd}(0)}$  diagram (Fig. 8) and compared with relevant end-members,  
487 including the Precambrian units of the Guiana Shield, the Jurassic mafic dykes related to the  
488 CAMP, marine sediments of the Demerara rise and abyssal plain and Suspended Particulate  
489 Matters (SPM) transported by modern rivers draining the northern part of South America and the  
490 Andes, three groups can be distinguished based on their differences in  $\epsilon_{\text{Nd}(0)}$  values.

491 The first group includes the samples AR1-1 (Early Cretaceous), AR1-9 (Cenomanian)  
492 and AR1-23 (Late Campanian) and is characterized by  $\epsilon_{\text{Nd}(0)}$  values  $>-2.2$  close to the mean  $\epsilon_{\text{Nd}(0)}$   
493 value of the Jurassic mafic dykes (JMD) (i.e. mean= 0.4 Standard Deviation= 3.1, Table S1  
494 (Deckart et al., 2005; Min et al., 2013) and close to Precambrian Avanavero Mafic Intrusions  
495 (PMI) (Hebeda et al., 1973; Leal et al., 2012), and some tholeiitic and komatiitic rocks of the  
496 Paleoproterozoic greenstone belts (GB) (Gruau et al., 1985; Kaminsky et al., 2004; McReath and  
497 Faraco, 2005; Voicu et al., 2000) (Figs. 3 and 9). Hence, these high  $\epsilon_{\text{Nd}(0)}$  values could indicate  
498 provenance from Precambrian or Jurassic mafic source outcropping in the northernmost parts of  
499 the Guiana Shield. Alternatively, these high  $\epsilon_{\text{Nd}(0)}$  values could also attest to the presence of  
500 active basic volcanism during the deposition of analyzed samples.

501 The two oldest Early Cretaceous (AR1-1) and Cenomanian (AR1-9) samples have trace  
502 elements ratios typical of “basic” sediments (i.e., sediments derived from a basic source *sensu*  
503 Cullers (2000)), with  $\text{Eu}/\text{Eu}^* >0.70$ ,  $\text{Th}/\text{Sc} <0.4$  and  $\text{Cr}/\text{Th} > 22.2$  (Table 3 and Fig. 6). From a  
504 geochemical point of view, it is not possible to distinguish between the Precambrian or Jurassic  
505 mafic rocks outcropping in the Guiana Shield and basic volcanism originated from the CLIP,  
506 Bahamas hot spot or Apoteri volcanism from the Takutu rift. The AR1-9 sample is marked by a  
507 positive  $\epsilon_{\text{Nd}(0)}$  excursions of +17.8 to 18.2 units when compared with overlying AR1-8 and  
508 underlying AR1-10 samples respectively (Fig. 6 and Table 4). We believe that these positive

509  $\epsilon_{Nd(0)}$  excursions sample cannot be explained by a contribution of Precambrian or Jurassic mafic  
510 rocks of the Guiana Shield and may favor a basic volcanic source for AR1-9 sample. In effect,  
511 Precambrian and Jurassic mafic rocks of the Guiana Shield always outcrop as patches in more  
512 differentiated magmatic rocks (Fig. 3) and it is likely that admixture of sediments derived from  
513 mafic and more differentiated sources would have resulted in a more negative  $\epsilon_{Nd(0)}$  value for  
514 AR1-9 sample. In addition, if mafic rocks outcropping in the Guiana Shield would have been  
515 eroded alone, the process leading to the erosion of these rocks would have to be progressive and  
516 this would be reflected by a progressive shift toward the highest  $\epsilon_{Nd(0)}$  values and not a positive  
517  $\epsilon_{Nd(0)}$  excursions of +17.8 to 18.2 units. Hence, we favor a Cenomanian basaltic volcanic source  
518 for sample AR1-9. Potential candidates may include the basic volcanism of the Caribbean Large  
519 Igneous Province (CLIP) active between 94 and 63 Ma (Loewen et al., 2013), or the basic  
520 volcanism of the Apoteri volcanic Formation outcropping in the Takutu rift (Crawford et al.,  
521 1985). Regarding the latter potential source, Proterozoic or Jurassic ages are generally ascribed  
522 to the basaltic flows (Crawford et al., 1985). However, two K/Ar dating measured on basaltic  
523 lava flows yield Early Cretaceous ages at  $114 \pm 3$  Ma and  $116 \pm 4$  Ma (Berrangé and Dearnley,  
524 1975,) so that a Cretaceous age for the Apoteri basaltic flow might be possible. However, a  
525 volcanic basaltic source might not be true for the oldest Early Cretaceous sample AR1-1. This  
526 sample is the only sample analyzed below the Late Albian unconformity (Figs 2 and 6) and  
527 because of this low sampling resolution, it is not possible to discard a progressive shift of  $\epsilon_{Nd(0)}$   
528 values. Hence, both contemporaneous basic volcanic rocks and mafic rocks of the Guiana Shield  
529 are possible sources for this sample. Potential volcanic source for this sample include the basic  
530 volcanism from the CLIP or the Apoteri Formation as well as Aptian-Albian volcanism found on  
531 the Guinea Plateau (Olyphant et al., 2017).

532 The Late Campanian sample (AR1-23) has trace element ratios characteristics of felsic  
533 sediments *sensu* (Cullers, 2000) with  $\text{Eu}/\text{Eu}^* < 0.70$ ,  $\text{Th}/\text{Sc} > 0.64$  and  $\text{Cr}/\text{Th} < 14.9$  (Table 3 and  
534 Fig. 6). These exclude mafic sources or basic volcanism as potential sources for this sample and  
535 suggest an origin linked to a more acid volcanic activity. The only regional source for this acid  
536 volcanism would be the pyroclastic flow recorded in the upper part of the Takutu Formation of  
537 the Takutu basin (Crawford et al., 1985). These pyroclastic flows have up to 87% of  $\text{SiO}_2$   
538 content but have never been dated. In fact, there is no radiometric nor biostratigraphic dating for  
539 the Takutu Formation and for the underlying and overlying formations. Even the positions of the  
540 Jurassic/Cretaceous and Cretaceous/Cenozoic boundaries are not constrained. Hence, a Late  
541 Cretaceous age for the Takutu Formation cannot be excluded and, in the absence of other option,  
542 the pyroclastic flows mentioned at the top of the formation could be the source of the Late  
543 Campanian sample.

544 The second group consists of AR1-11E (Cenomanian) and AR1-21 (Santonian-  
545 Campanian) samples and is characterized by intermediate  $\epsilon_{\text{Nd}(0)}$  values (-12.2 and -13.6  
546 respectively, Figs. 6 and 8 and Table 4). In the case of Amazonian sediments, this  $\epsilon_{\text{Nd}(0)}$  value is  
547 generally used as a cutoff value for identifying more radiogenic Andean-derived sediments  
548 (Figueiredo et al., 2009; Horbe et al., 2014; Hurtado et al., 2018; Roddaz et al., 2005). The Sr-Nd  
549 isotopic composition of Amazonian Andean sediments is commonly interpreted to reflect mixing  
550 between two end-members: the juvenile primitive Andean Arc and the older upper continental  
551 crust of the Brazilian shield (Basu et al., 1990; Roddaz et al., 2005). Applying this finding to our  
552 results suggests that the two analyzed samples with intermediate  $\epsilon_{\text{Nd}(0)}$  values might result from  
553 mixing between the northern mafic sources listed above (i.e., JMD, PMI and GB) or basic  
554 volcanic sources (CLIP, Bahamas hot spot or Apoteri volcanism) and the differentiated

555 Precambrian granitoids and metamorphic rocks (e.g., PGGF, PHGB) (Fig. 8). However, more  
556 samples are needed to test a mixing hyperbole between these two end-members.

557 The third group of samples encompasses all other analyzed and is characterized by  $\epsilon_{\text{Nd}(0)}$   
558 values inferior to -15.8 with a median  $\epsilon_{\text{Nd}(0)}$  value at -19.2 (Table 4, Fig. 8). Such low  $\epsilon_{\text{Nd}(0)}$   
559 values are typical of Amazonian cratonic-derived sedimentary rocks and present-day cratonic-  
560 derived river sediments (e.g., Maroni, upper Orinoco, Trombetas rivers) dominated by supplies  
561 from Paleoproterozoic and Mesoproterozoic granites, gneiss and metamorphic series (PFFG)  
562 covering the more inner parts of the craton (Figs. 3 and 8) (Allègre et al., 1996; Goldstein et al.  
563 1997; Bayon et al., 2015; Figueiredo et al., 2009; Roddaz et al., 2005). For instance, Suspended  
564 Particulate Matter (SPM) transported by the Maroni River draining the Paleoproterozoic terranes  
565 to the east of the Guiana shield have  $\epsilon_{\text{Nd}(0)}$  values between -21 and -25.2 (Rousseau et al., 2019)  
566 (Fig. 3 and 8). Compared with the modern Maroni SPM, the Cretaceous sediments from the  
567 Guyana-Suriname basin have a slightly more juvenile Nd isotopic ratios but they have similar  
568  $\epsilon_{\text{Nd}(0)}$  values as the Upper Orinoco river fine-grained sediments analyzed in Goldstein et al. 1997  
569 (-19.6 and -20.5 respectively, Table S1) suggesting a similar origin (Fig. 3).

570 Based on their  $\epsilon_{\text{Nd}(0)}$  values, most of the analyzed samples derive from the Guiana Shield  
571 with variable contributions from two main sources: 1) Paleoproterozoic granitic and  
572 metamorphic units covering the innermost parts of the shield and 2) Jurassic or Precambrian  
573 mafic dykes and greenstone belts. More insight can be gained with trace elements ratios and  
574  $^{87}\text{Sr}/^{86}\text{Sr}$  isotopic ratios. For instance, the four Late Santonian to Paleocene samples have more  
575 radiogenic  $^{87}\text{Sr}/^{86}\text{Sr}$  ratios than the oldest samples. These younger samples have Eu/Eu\*, Th/Sc  
576 and Cr/Th ratios close to that of the PAAS whereas oldest samples have Eu/Eu\*, Th/Sc and  
577 Cr/Th ratios close to those defining “basic sediments” sensu Cullers (2000) (Fig. 6). As there is

578 no coeval change in  $\epsilon_{\text{Nd}(0)}$  values, these temporal changes in trace elements ratios and  $^{87}\text{Sr}/^{86}\text{Sr}$   
579 isotopic ratios could result from increasing contributions of more felsic sources rather than  
580 contribution from older sources. Potential candidates for these felsic sources could be  
581 Paleoproterozoic granitoids, gneiss and felsic volcanic units, Mezoproterozoic granites, or high-  
582 grade granulite belts (PGGF, MG, PHGB in Fig. 3 respectively). Both units outcrop in the inner  
583 part of the Guiana Shield and thus imply an extension of the drainage area toward the South  
584 between the Coniacian and the Santonian (Fig. 9).

### 585 5.3 Implications for the Late Cretaceous evolution of Atlantic equatorial margins

586 Our geochemical data support that Early Cretaceous-Paleocene sediments of the Guyana-  
587 Suriname basin have a Guiana cratonic provenance. Analysis of 2D seismic lines suggest that the  
588 deep offshore part of the Guyana-Suriname basin was supplied by these cratonic sediments via a  
589 large canyon system fed by the proto-Berbice river (Figs.1 and 9) with a paleo-delta probably  
590 located between the present-day Berbice and Corantijn rivers (Erlich and Keens-Dumas 2007;  
591 Mourlot, 2018; Yang and Escalona, 2011). Our provenance data also suggests an extension of  
592 the proto-Berbice drainage area toward the inner parts of the Guiana craton after the Coniacian  
593 (~86 Ma, Fig. 9), likely through the Takutu rift. This provenance change was associated with a  
594 decrease in TOC content and a six fold increase in sedimentation rate in the Arapaima-1 well  
595 (Mourlot, 2018), suggesting increasing erosion of inner parts of the Guiana Shield.  
596 Geomorphological and thermochronological data also attest to uplift and erosion of the inner  
597 domains of the Guiana Shield during the Late Cretaceous (Sapin et al., 2016). In the easternmost  
598 part of Suriname and in Brazil (close to the Brazilian-Suriname frontier) (see Fig. 7 in Sapin et  
599 al., 2016), a Late Cretaceous erosive surface (“peneplanation surface”) termed S0 exposed at  
600 elevation  $> \sim 900$  m above sea level (asl) has been identified and mapped (Sapin et al., 2016).

601 This surface was dated by Ar/Ar on lateritic material at ~71 Ma and Apatite Fission Track  
602 Analysis at  $77 \pm 3$  Ma (Sapin et al., 2016 and references therein) suggesting that a significant  
603 erosion affected this part of the craton during the Campanian. This S0 surface outcrops  
604 immediately above the PGGF basement and hence has recorded the uplift and erosion of this  
605 terrane, which would be consistent with the increasing contribution of a felsic source to the Late  
606 Santonian-Paleocene sediments. This post Coniacian uplift of the Guiana Shield post-dated by  
607 >20 Ma the post-rift Albian tectonic inversion ascribed to a plate kinematic change that affected  
608 the Demerara Plateau (offshore French Guiana) at *ca* 105 Ma (Basile et al., 2013). In  
609 northeastern Brazil, various studies have presented evidences for a Late Cretaceous uplift  
610 (Harman et al., 1998; Morais Neto et al., 2009; Peulvast and Bétard, 2015; Potter, 1997).  
611 Increase of denudation at ~80–60 Ma of the eastern Central Brazilian shield is documented by  
612 thermal histories derived from fission track data (Harman et al., 1998). This uplift and erosion of  
613 the Central Brazilian shield is also attested by the development of the high elevated (~720 m asl)  
614 Brazilian Carajas surface in northeastern Amazonia which started its weathering history at *ca.* 80  
615 Ma (Monteiro et al., 2018). Late Cretaceous fission track cooling ages (Morais Neto et al., 2009)  
616 as well as presence of Cenomanian marine deposits associated to development of Paleogene  
617 laterites on the top of the Borborema Plateau (Peulvast and Bétard, 2015) indicate that the  
618 Borborema plateau (Northeastern Brazil) underwent uplift and denudation between the  
619 Cenomanian and Early Cenozoic. In the conjugate margin of NW Africa, the  
620 Campanian–Maastrichtian is characterized by increasing input of Precambrian detritus along the  
621 Northwest African Margin and a progression of drainage areas toward the east and the inner  
622 units of the West African Craton (Mourlot et al., 2018a).

623           Based on this literature review, both the northeastern South American and West African  
624 cratons experienced coeval post Coniacian uplift of their inner parts suggesting that a similar  
625 post-rift geodynamic mechanism occurred during the opening of the Atlantic Equatorial Ocean.  
626 This coeval uplift of the Atlantic margins could result from significant intracontinental  
627 deformation caused by major change in the relative plate motions between Africa, Antarctica,  
628 and South America that began between anomaly C34 (83 Ma) and C31 (67 Ma) (see Harman et  
629 al., 1998 and references therein) as well as mantle upwelling under the margin (Matton and  
630 Jébrak, 2009) or a combination of these. Furthermore, given the presence of a volcanic eruption  
631 in the Late Campanian as recorded by the sample AR1-23, the presence of an active plume  
632 mantle upwelling cannot be discarded.

## 633 **6. Conclusions**

634           Based on the TOC content,  $\delta^{13}\text{C}_{\text{TOC}}$  data, major and trace element concentrations and Sr–  
635 Nd isotopic compositions of Cretaceous to Paleocene sedimentary rocks sampled in the  
636 Arapaima-1 well (Guyana-Suriname basin) compared with an extensive Sr-Nd isotopic  
637 composition of possible sources, this provenance study yields the following conclusions:

- 638       • Three samples AR1-1 ((Early Cretaceous, AR1-9 (Cenomanian, ) and AR1-23 (Late  
639       Campanian in age) have  $\varepsilon_{\text{Nd}(0)}$  values  $>-2.2$  that might have recorded volcanic activity  
640       during their deposition. However, this interpretation might not be true for the oldest  
641       sample AR1-1 that could also be sourced by mafic rocks from the Guiana Shield. The  
642       Cenomanian sample may have recorded basic volcanic activity of the Caribbean Large  
643       Igneous Province or the Takutu rift, whereas the Late Campanian sample would record  
644       acid volcanic eruption associated with the pyroclastic flow having affected the Takutu rift  
645       in the Cretaceous;

- 646 • All other analyzed samples have an overall Guiana cratonic provenance with variable  
647 contributions from Paleoproterozoic and Mesoproterozoic and greenstone belt, Jurassic  
648 and Precambrian mafic dykes. Two Cenomanian and Santonian-Campanian samples  
649 (AR1-11F and AR1-21) have intermediate  $\epsilon_{Nd(0)}$  values of  $\sim -13$  suggesting more  
650 important contribution of mafic rocks from the Guiana Shield or basic volcanic rocks  
651 from the CLIP, Bahamas hot spot or Apoteri volcanism. The other samples have  $\epsilon_{Nd(0)} <$   
652  $-15.8$  and suggest a dominant provenance from the inner Paleoproterozoic granitic units of  
653 the Guiana Shield;
- 654 • Late Santonian to Paleocene samples have more radiogenic  $^{87}Sr/^{86}Sr$  isotopic ratios and  
655 trace element ratios characteristic of more differentiated sources when compared with  
656 oldest samples. This suggests an increasing contribution from the Paleoproterozoic  
657 granitoids, gneiss and felsic volcanism units or the Mesoproterozoic granites through  
658 time. This also implies an evolution of the drainage area toward the inner parts of the  
659 Guiana Shield between the Coniacian and the Santonian.

660 This post-Coniacian erosion of the inner parts of the Guiana Shield is recorded in various  
661 other parts of the northeastern South American and West African cratons. This suggests that  
662 they experienced a similar uplift mechanism occurring during the opening of the Atlantic  
663 Equatorial Ocean. Probable causes could be a major change in the relative plate motions  
664 between Africa and South America as well as post rift mantle upwelling under the margin.  
665 The latter hypothesis could be favored by the supposed presence of active volcanism during  
666 the deposition of the analyzed samples.

667 **Acknowledgments**

668 This study was funded by Total Exploration and Production through the R&D project  
669 “Sedimentology of organic matter in deep oceanic basins” (TOTAL: FR00007862 and CNRS  
670 122560). Jung-Hyun Kim was also partly supported by a grant from the National Research  
671 Foundation of Korea (NRF) funded by the Korea government (MSIP) (No.2016R1A2B3015388)  
672 and a project from the Korean Government (MSIT) (NRF-2015M1A5A1037243, KOPRI-  
673 PN20090). This work was part of Yannick Murlot PhD thesis funded by Total E&P. We thank  
674 three anonymous reviewers as well as the editor Adina Paytan for valuable reviews that  
675 improved this contribution.

676

677 **Data availability**

678 All geochemical data including total organic carbon (TOC) content,  $\delta^{13}\text{C}_{\text{TOC}}$ , major and trace  
679 element concentrations, and Sr-Nd isotopic data (Table 2 to 4) as well as compiled database,  
680 major and trace element uncertainties and correlation coefficients (Table S1 to S3) are uploaded  
681 into an online supplementary dataset associated with this paper (Roddaz, Martin; Dera,  
682 Guillaume; Murlot, Yannick; Calves, Gerome; Kim, Jung-Hyun; Chaboureau, Anne-Claire;  
683 Mounic, Stephanie; Raison, Francois (2020), “Geochemistry of Arapaima well sediments  
684 Roddaz et al. in Revision to Marine Geology”, Mendeley Data, V2, doi: 10.17632/jnwgsn98tt.2,  
685 <http://dx.doi.org/10.17632/jnwgsn98tt.2> ).

686 **References**

687 Algeo, T.J., Liu, J., 2020. A re-assessment of elemental proxies for paleoredox analysis. *Chem.*  
688 *Geol.* 540, 119549. <https://doi.org/10.1016/j.chemgeo.2020.119549>

689 Allègre, C.J., Dupré, B., Nègre, P., Gaillardet, J., 1996. Sr–Nd–Pb isotope systematics in  
690 Amazon and Congo River systems: constraints about erosion processes. *Chem. Geol.*  
691 131, 93–112. [https://doi.org/10.1016/0009-2541\(96\)00028-9](https://doi.org/10.1016/0009-2541(96)00028-9)

692 Andersen, T., Elburg, M.A., Magwaza, B.N., 2019. Sources of bias in detrital zircon  
693 geochronology: Discordance, concealed lead loss and common lead correction. *Earth-Sci.*  
694 *Rev.* 197, 102899. <https://doi.org/10.1016/j.earscirev.2019.102899>

695 Barreto, C.J.S., Lafon, J.M., da Rosa Costa, L.T., Dantas, E.L., 2013. Paleoproterozoic granitoids  
696 from the northern limit of the Archean Amapá block (Brazil), southeastern Guyana  
697 Shield: Pb–Pb evaporation in zircons and Sm–Nd geochronology. *J. South Am. Earth Sci.*  
698 45, 97–116. <https://doi.org/10.1016/j.jsames.2013.02.005>

699 Basile, C., 2015. Transform continental margins — part 1: Concepts and models. *Tectonophysics*  
700 661, 1–10. <https://doi.org/10.1016/j.tecto.2015.08.034>

701 Basile, C., Girault, I., Paquette, J.-L., Agranier, A., Loncke, L., Heuret, A., Poetisi, E., 2020. The  
702 Jurassic magmatism of the Demerara Plateau (offshore French Guiana) as a remnant of  
703 the Sierra Leone hotspot during the Atlantic rifting. *Sci. Rep.* 10, 7486.  
704 <https://doi.org/10.1038/s41598-020-64333-5>

705 Basile, C., Maillard, A., Patriat, M., Gaullier, V., Loncke, L., Roest, W., Mercier de Lépinay, M.,  
706 Pattier, F., 2013. Structure and evolution of the Demerara Plateau, offshore French  
707 Guiana: Rifting, tectonic inversion and post-rift tilting at transform–divergent margins  
708 intersection. *Tectonophysics, Basin Dynamics* 591, 16–29.  
709 <https://doi.org/10.1016/j.tecto.2012.01.010>

710 Basile, C., Mascle, J., Guiraud, R., 2005. Phanerozoic geological evolution of the Equatorial  
711 Atlantic domain. *J. Afr. Earth Sci., Phanerozoic Evolution of Africa* 43, 275–282.  
712 <https://doi.org/10.1016/j.jafrearsci.2005.07.011>

713 Basu, A.R., Sharma, M., DeCelles, P.G., 1990. Nd, Sr-isotopic provenance and trace element  
714 geochemistry of Amazonian foreland basin fluvial sands, Bolivia and Peru: implications  
715 for ensialic Andean orogeny. *Earth Planet. Sci. Lett.* 100, 1–17.  
716 [https://doi.org/10.1016/0012-821X\(90\)90172-T](https://doi.org/10.1016/0012-821X(90)90172-T)

717 Bayon, G., German, C.R., Boella, R.M., Milton, J.A., Taylor, R.N., Nesbitt, R.W., 2002. An  
718 improved method for extracting marine sediment fractions and its application to Sr and  
719 Nd isotopic analysis. *Chem. Geol.* 187, 179–199. [https://doi.org/10.1016/S0009-](https://doi.org/10.1016/S0009-2541(01)00416-8)  
720 [2541\(01\)00416-8](https://doi.org/10.1016/S0009-2541(01)00416-8)

721 Bayon, G., Toucanne, S., Skonieczny, C., André, L., Bermell, S., Cheron, S., Dennielou, B.,  
722 Etoubleau, J., Freslon, N., Gauchery, T., Germain, Y., Jorry, S.J., Ménot, G., Monin, L.,  
723 Ponzevera, E., Rouget, M.-L., Tachikawa, K., Barrat, J.A., 2015. Rare earth elements and  
724 neodymium isotopes in world river sediments revisited. *Geochim. Cosmochim. Acta* 170,  
725 17–38. <https://doi.org/10.1016/j.gca.2015.08.001>

726 Benkhelil, J., Mascle, J., Tricart, P., 1995. The Guinea continental margin: an example of a  
727 structurally complex transform margin. *Tectonophysics* 248, 117–137.  
728 [https://doi.org/10.1016/0040-1951\(94\)00246-6](https://doi.org/10.1016/0040-1951(94)00246-6)

729 Berrangé, J.P., Dearnley, R., 1975. The Apoteri volcanic formation — tholeiitic flows in the  
730 North Savannas Graben of Guyana and Brazil. *Geol. Rundsch.* 64, 883–899.  
731 <https://doi.org/10.1007/BF01820702>

- 732 Berrocoso, Á.J., MacLeod, K.G., Calvert, S.E., Elorza, J., 2008. Bottom water anoxia,  
733 inoceramid colonization, and benthopelagic coupling during black shale deposition on  
734 Demerara Rise (Late Cretaceous western tropical North Atlantic). *Paleoceanography* 23.  
735 <https://doi.org/10.1029/2007PA001545>
- 736 Bodin, S., Meissner, P., Janssen, N.M.M., Steuber, T., Mutterlose, J., 2015. Large igneous  
737 provinces and organic carbon burial: Controls on global temperature and continental  
738 weathering during the Early Cretaceous. *Glob. Planet. Change* 133, 238–253.  
739 <https://doi.org/10.1016/j.gloplacha.2015.09.001>
- 740 Boher, M., Abouchami, W., Michard, A., Albarede, F., Arndt, N.T., 1992. Crustal growth in  
741 West Africa at 2.1 Ga. *J. Geophys. Res. Solid Earth* 97, 345–369.  
742 <https://doi.org/10.1029/91JB01640>
- 743 Bouchez, J., Gaillardet, J., France- Lanord, C., Maurice, L., Dutra- Maia, P., 2011. Grain size  
744 control of river suspended sediment geochemistry: Clues from Amazon River depth  
745 profiles. *Geochem. Geophys. Geosystems* 12. <https://doi.org/10.1029/2010GC003380>
- 746 Caracciolo, L., 2020. Sediment generation and sediment routing systems from a quantitative  
747 provenance analysis perspective: Review, application and future development. *Earth-Sci.*  
748 *Rev.* 209, 103226. <https://doi.org/10.1016/j.earscirev.2020.103226>
- 749 Chew, D., O’Sullivan, G., Caracciolo, L., Mark, C., Tyrrell, S., 2020. Sourcing the sand:  
750 Accessory mineral fertility, analytical and other biases in detrital U-Pb provenance  
751 analysis. *Earth-Sci. Rev.* 202, 103093. <https://doi.org/10.1016/j.earscirev.2020.103093>
- 752 Clift, P.D., Blusztajn, J., 2005. Reorganization of the western Himalayan river system after five  
753 million years ago. *Nature* 438, 1001–1003. <https://doi.org/10.1038/nature04379>

754 Cogné, N., Gallagher, K., Cobbold, P.R., Riccomini, C., Gautheron, C., 2012. Post-breakup  
755 tectonics in southeast Brazil from thermochronological data and combined inverse-  
756 forward thermal history modeling. *J. Geophys. Res. Solid Earth* 117.  
757 <https://doi.org/10.1029/2012JB009340>

758 Condie, K.C., 1993. Chemical composition and evolution of the upper continental crust:  
759 Contrasting results from surface samples and shales. *Chem. Geol.* 104, 1–37.  
760 [https://doi.org/10.1016/0009-2541\(93\)90140-E](https://doi.org/10.1016/0009-2541(93)90140-E)

761 Crawford, F.D., Szelewski, C.E., Alvey, G.D., 1985. Geology and Exploration in the Takutu  
762 Graben of Guyana Brazil. *J. Pet. Geol.* 8, 5–36. [https://doi.org/10.1111/j.1747-](https://doi.org/10.1111/j.1747-5457.1985.tb00189.x)  
763 [5457.1985.tb00189.x](https://doi.org/10.1111/j.1747-5457.1985.tb00189.x)

764 Cullers, R.L., 2000. The geochemistry of shales, siltstones and sandstones of Pennsylvanian–  
765 Permian age, Colorado, USA: implications for provenance and metamorphic studies.  
766 *Lithos* 51, 181–203. [https://doi.org/10.1016/S0024-4937\(99\)00063-8](https://doi.org/10.1016/S0024-4937(99)00063-8)

767 da Rosa-Costa, L.T., Lafon, J.M., Delor, C., 2006. Zircon geochronology and Sm–Nd isotopic  
768 study: Further constraints for the Archean and Paleoproterozoic geodynamical evolution  
769 of the southeastern Guiana Shield, north of Amazonian Craton, Brazil. *Gondwana Res.*  
770 10, 277–300. <https://doi.org/10.1016/j.gr.2006.02.012>

771 De Baar, H.J.W., Bacon, M.P., Brewer, P.G., Bruland, K.W., 1985. Rare earth elements in the  
772 Pacific and Atlantic Oceans. *Geochim. Cosmochim. Acta* 49, 1943–1959.  
773 [https://doi.org/10.1016/0016-7037\(85\)90089-4](https://doi.org/10.1016/0016-7037(85)90089-4)

774 Deckart, K., Bertrand, H., Liégeois, J.-P., 2005. Geochemistry and Sr, Nd, Pb isotopic  
775 composition of the Central Atlantic Magmatic Province (CAMP) in Guyana and Guinea.

776 Lithos, Isotopes in Igneous Petrogenesis 82, 289–314.  
777 <https://doi.org/10.1016/j.lithos.2004.09.023>

778 Dera, G., Prunier, J., Smith, P.L., Haggart, J.W., Popov, E., Guzhov, A., Rogov, M., Delsate, D.,  
779 Thies, D., Cuny, G., Pucéat, E., Charbonnier, G., Bayon, G., 2015. Nd isotope constraints  
780 on ocean circulation, paleoclimate, and continental drainage during the Jurassic breakup  
781 of Pangea. *Gondwana Res.* 27, 1599–1615. <https://doi.org/10.1016/j.gr.2014.02.006>

782 Dickinson, W.R., 2008. Impact of differential zircon fertility of granitoid basement rocks in  
783 North America on age populations of detrital zircons and implications for granite  
784 petrogenesis. *Earth Planet. Sci. Lett.* 275, 80–92.  
785 <https://doi.org/10.1016/j.epsl.2008.08.003>

786 Dickinson, W.R., 1985. Interpreting Provenance Relations from Detrital Modes of Sandstones,  
787 in: Zuffa, G.G. (Ed.), *Provenance of Arenites*, NATO ASI Series. Springer Netherlands,  
788 Dordrecht, pp. 333–361. [https://doi.org/10.1007/978-94-017-2809-6\\_15](https://doi.org/10.1007/978-94-017-2809-6_15)

789 Dickinson, W.R., Suczek, C.A., 1979. Plate Tectonics and Sandstone Compositions. *AAPG Bull.*  
790 63, 2164–2182. <https://doi.org/10.1306/2F9188FB-16CE-11D7-8645000102C1865D>

791 Donnadiou, Y., Pucéat, E., Moiroud, M., Guillocheau, F., Deconinck, J.-F., 2016. A better-  
792 ventilated ocean triggered by Late Cretaceous changes in continental configuration. *Nat.*  
793 *Commun.* 7, 1–12. <https://doi.org/10.1038/ncomms10316>

794 Emery, K.O., Uchupi, E., Phillips, J., Bowin, C., Mascle, J., 1975. Continental Margin Off  
795 Western Africa: Angola to Sierra Leone. *AAPG Bull.* 59, 2209–2265.  
796 <https://doi.org/10.1306/83D92249-16C7-11D7-8645000102C1865D>

797 Erlich, R.N., Fallon, J., O’Sullivan, P., 2018. Stratigraphy and LA-ICP-MS zircon U-PB  
798 provenance of middle Permian to Maastrichtian sandstones from outcrop and subsurface

799 control in the sub-Andean basins of Peru, in: Petroleum Basins and Hydrocarbon  
800 Potential of the Andes of Peru and Bolivia, AAPG Memoirs. AAPG, pp. 175–222.

801 Fedo, C.M., Nesbitt, H.W., Young, G.M., 1995. Unraveling the effects of potassium  
802 metasomatism in sedimentary rocks and paleosols, with implications for paleoweathering  
803 conditions and provenance. *Geology* 23, 921–924. [https://doi.org/10.1130/0091-](https://doi.org/10.1130/0091-7613(1995)023<0921:UTEOPM>2.3.CO;2)  
804 [7613\(1995\)023<0921:UTEOPM>2.3.CO;2](https://doi.org/10.1130/0091-7613(1995)023<0921:UTEOPM>2.3.CO;2)

805 Figueiredo, J., Hoorn, C., Ven, P. van der, Soares, E., 2009. Late Miocene onset of the Amazon  
806 River and the Amazon deep-sea fan: Evidence from the Foz do Amazonas Basin.  
807 *Geology* 37, 619–622. <https://doi.org/10.1130/G25567A.1>

808 Friedrich, O., Norris, R.D., Erbacher, J., 2012. Evolution of middle to Late Cretaceous oceans—  
809 A 55 m.y. record of Earth’s temperature and carbon cycle. *Geology* 40, 107–110.  
810 <https://doi.org/10.1130/G32701.1>

811 Gallagher, K., Brown, R., 1999. The Mesozoic denudation history of the Atlantic margins of  
812 southern Africa and southeast Brazil and the relationship to offshore sedimentation. *Geol.*  
813 *Soc. Lond. Spec. Publ.* 153, 41–53. <https://doi.org/10.1144/GSL.SP.1999.153.01.03>

814 Gallagher, K., Hawkesworth, C.J., Mantovani, M.S.M., 1994. The denudation history of the  
815 onshore continental margin of SE Brazil inferred from apatite fission track data. *J.*  
816 *Geophys. Res. Solid Earth* 99, 18117–18145. <https://doi.org/10.1029/94JB00661>

817 Garzanti, E., 2019. Petrographic classification of sand and sandstone. *Earth-Sci. Rev.* 192, 545–  
818 563. <https://doi.org/10.1016/j.earscirev.2018.12.014>

819 Garzanti, E., 2016. From static to dynamic provenance analysis—Sedimentary petrology  
820 upgraded. *Sediment. Geol., Sediment generation and provenance: processes and*  
821 *pathways* 336, 3–13. <https://doi.org/10.1016/j.sedgeo.2015.07.010>

822 Garzanti, E., Andò, S., 2019. Heavy Minerals for Junior Woodchucks. *Minerals* 9, 148.  
823 <https://doi.org/10.3390/min9030148>

824 Garzanti, E., Andò, S., Vezzoli, G., 2009. Grain-size dependence of sediment composition and  
825 environmental bias in provenance studies. *Earth Planet. Sci. Lett.* 277, 422–432.  
826 <https://doi.org/10.1016/j.epsl.2008.11.007>

827 Garzanti, E., Andò, S., Vezzoli, G., 2008. Settling equivalence of detrital minerals and grain-size  
828 dependence of sediment composition. *Earth Planet. Sci. Lett.* 273, 138–151.  
829 <https://doi.org/10.1016/j.epsl.2008.06.020>

830 Garzanti, E., Padoan, M., Setti, M., López-Galindo, A., Villa, I.M., 2014. Provenance versus  
831 weathering control on the composition of tropical river mud (southern Africa). *Chem.*  
832 *Geol.* 366, 61–74. <https://doi.org/10.1016/j.chemgeo.2013.12.016>

833 Gaudette, H.E., Mendoza, V., Hurley, P.M., Fairbairn, H.W., 1978. Geology and age of the  
834 Parguaza rapakivi granite, Venezuela. *GSA Bull.* 89, 1335–1340.  
835 [https://doi.org/10.1130/0016-7606\(1978\)89<1335:GAAOTP>2.0.CO;2](https://doi.org/10.1130/0016-7606(1978)89<1335:GAAOTP>2.0.CO;2)

836 Gaudette, H.E., Olszewski, W.J., Santos, J.O.S., 1996. Geochronology of Precambrian rocks  
837 from the northern part of the Guiana Shield, State of Roraima, Brazil. *J. South Am. Earth*  
838 *Sci.* 9, 183–195. [https://doi.org/10.1016/0895-9811\(96\)00005-3](https://doi.org/10.1016/0895-9811(96)00005-3)

839 George, S.W.M., Horton, B.K., Jackson, L.J., Moreno, F., Carlotto, V., Garziane, C.N., 2019.  
840 Chapter 10 - Sediment provenance variations during contrasting Mesozoic-early  
841 Cenozoic tectonic regimes of the northern Peruvian Andes and Santiago-Marañón  
842 foreland basin, in: Horton, B.K., Folguera, A. (Eds.), *Andean Tectonics*. Elsevier, pp.  
843 269–296. <https://doi.org/10.1016/B978-0-12-816009-1.00012-5>

844 Gibbs, A.K., Montgomery, C.W., O'Day, P.A., Erslev, E.A., 1986. The Archean-Proterozoic  
845 transition: Evidence from the geochemistry of metasedimentary rocks of Guyana and  
846 Montana. *Geochim. Cosmochim. Acta* 50, 2125–2141. [https://doi.org/10.1016/0016-](https://doi.org/10.1016/0016-7037(86)90067-0)  
847 [7037\(86\)90067-0](https://doi.org/10.1016/0016-7037(86)90067-0)

848 Goldstein, S.L., Arndt, N.T., Stallard, R.F., 1997. The history of a continent from U–Pb ages of  
849 zircons from Orinoco River sand and Sm–Nd isotopes in Orinoco basin river sediments.  
850 *Chem. Geol.* 139, 271–286. [https://doi.org/10.1016/S0009-2541\(97\)00039-9](https://doi.org/10.1016/S0009-2541(97)00039-9)

851 Gouyet, S., Unternehr, P., Mascle, A., 1994. The French Guyana Margin and the Demerara  
852 Plateau: Geological History and Petroleum Plays, in: Mascle, Alain (Ed.), *Hydrocarbon*  
853 *and Petroleum Geology of France*, Special Publication of the European Association of  
854 *Petroleum Geoscientists*. Springer, Berlin, Heidelberg, pp. 411–422.  
855 [https://doi.org/10.1007/978-3-642-78849-9\\_29](https://doi.org/10.1007/978-3-642-78849-9_29)

856 Gruau, G., Martin, H., Leveque, B., Capdevila, R., Marot, A., 1985. Rb–Sr and Sm–Nd  
857 geochronology of lower Proterozoic granite–greenstone terrains in French Guiana,  
858 South America. *Precambrian Res.* 30, 63–80. [https://doi.org/10.1016/0301-](https://doi.org/10.1016/0301-9268(85)90029-4)  
859 [9268\(85\)90029-4](https://doi.org/10.1016/0301-9268(85)90029-4)

860 Hall, S.A., Bird, D.E., McLean, D.J., Towle, P.J., Grant, J.V., Danque, H.A., 2018. New  
861 constraints on the age of the opening of the South Atlantic basin. *Mar. Pet. Geol.* 95, 50–  
862 66. <https://doi.org/10.1016/j.marpetgeo.2018.03.010>

863 Harman, R., Gallagher, K., Brown, R., Raza, A., Bizzi, L., 1998. Accelerated denudation and  
864 tectonic/geomorphic reactivation of the cratons of northeastern Brazil during the Late  
865 Cretaceous. *J. Geophys. Res. Solid Earth* 103, 27091–27105.  
866 <https://doi.org/10.1029/98JB02524>

867 Hebeda, E.H., Boelrijk, N.A.I.M., Priem, H.N.A., Verdurmen, E.A.Th., Verschure, R.H., 1973.  
868 Excess radiogenic argon in the Precambrian Avanavero Dolerite in western Suriname  
869 (South America). *Earth Planet. Sci. Lett.* 20, 189–200. [https://doi.org/10.1016/0012-](https://doi.org/10.1016/0012-821X(73)90157-X)  
870 [821X\(73\)90157-X](https://doi.org/10.1016/0012-821X(73)90157-X)

871 Heine, C., Zoethout, J., Müller, R.D., 2013. Kinematics of the South Atlantic rift. *Solid Earth* 4,  
872 215–253. <https://doi.org/10.5194/se-4-215-2013>

873 Heinonen, A.P., Fraga, L.M., Rämö, O.T., Dall’Agnol, R., Mänttari, I., Andersen, T., 2012.  
874 Petrogenesis of the igneous Mucajaí AMG complex, northern Amazonian craton —  
875 Geochemical, U–Pb geochronological, and Nd–Hf–O isotopic constraints. *Lithos, A-type*  
876 *granites and related rocks through time* 151, 17–34.  
877 <https://doi.org/10.1016/j.lithos.2011.07.016>

878 Hetzel, A., Böttcher, M.E., Wortmann, U.G., Brumsack, H.-J., 2009. Paleo-redox conditions  
879 during OAE 2 reflected in Demerara Rise sediment geochemistry (ODP Leg 207).  
880 *Palaeogeogr. Palaeoclimatol. Palaeoecol., Organic-carbon-rich sediments through the*  
881 *Phanerozoic: Processes, progress, and perspectives* 273, 302–328.  
882 <https://doi.org/10.1016/j.palaeo.2008.11.005>

883 Hiruma, S.T., Riccomini, C., Modenesi-Gauttieri, M.C., Hackspacher, P.C., Neto, J.C.H.,  
884 Franco-Magalhães, A.O.B., 2010. Denudation history of the Bocaina Plateau, Serra do  
885 Mar, southeastern Brazil: Relationships to Gondwana breakup and passive margin  
886 development. *Gondwana Res.* 18, 674–687. <https://doi.org/10.1016/j.gr.2010.03.001>

887 Hodell, D.A., Kamenov, G.D., Hathorne, E.C., Zachos, J.C., Röhl, U., Westerhold, T., 2007.  
888 Variations in the strontium isotope composition of seawater during the Paleocene and

889 early Eocene from ODP Leg 208 (Walvis Ridge). *Geochem. Geophys. Geosystems* 8.  
890 <https://doi.org/10.1029/2007GC001607>

891 Horbe, A.M.C., da Trindade, I.R., Dantas, E.L., Santos, R.V., Roddaz, M., 2014. Provenance of  
892 quaternary and modern alluvial deposits of the Amazonian floodplain (Brazil) inferred  
893 from major and trace elements and Pb–Nd–Sr isotopes. *Palaeogeogr. Palaeoclimatol.*  
894 *Palaeoecol.* 411, 144–154. <https://doi.org/10.1016/j.palaeo.2014.06.019>

895 Huck, C.E., Fliedert, T. van de, Jiménez- Espejo, F.J., Bohaty, S.M., Röhl, U., Hammond, S.J.,  
896 2016. Robustness of fossil fish teeth for seawater neodymium isotope reconstructions  
897 under variable redox conditions in an ancient shallow marine setting. *Geochem. Geophys.*  
898 *Geosystems* 17, 679–698. <https://doi.org/10.1002/2015GC006218>

899 Hurley, P.M., Melcher, G.C., Pinson Jr., W.H., Fairbairn, H.W., 1968. Some orogenic episodes  
900 in South America by K–Ar and whole-rock Rb–Sr dating. *Can. J. Earth Sci.* 5, 633–638.  
901 <https://doi.org/10.1139/e68-059>

902 Hurtado, C., Roddaz, M., Santos, R.V., Baby, P., Antoine, P.-O., Dantas, E.L., 2018. Cretaceous-  
903 early Paleocene drainage shift of Amazonian rivers driven by Equatorial Atlantic Ocean  
904 opening and Andean uplift as deduced from the provenance of northern Peruvian  
905 sedimentary rocks (Huallaga basin). *Gondwana Res.* 63, 152–168.  
906 <https://doi.org/10.1016/j.gr.2018.05.012>

907 Jacobsen, S.B., Wasserburg, G.J., 1980. Sm-Nd isotopic evolution of chondrites. *Earth Planet.*  
908 *Sci. Lett.* 50, 139–155. [https://doi.org/10.1016/0012-821X\(80\)90125-9](https://doi.org/10.1016/0012-821X(80)90125-9)

909 Japsen, P., Bonow, J.M., Green, P.F., Cobbold, P.R., Chiossi, D., Lilletveit, R., Magnavita, L.P.,  
910 Pedreira, A., 2012. Episodic burial and exhumation in NE Brazil after opening of the  
911 South Atlantic. *GSA Bull.* 124, 800–816. <https://doi.org/10.1130/B30515.1>

912 Jeandel, C., Arsouze, T., Lacan, F., Téchiné, P., Dutay, J.-C., 2007. Isotopic Nd compositions  
913 and concentrations of the lithogenic inputs into the ocean: A compilation, with an  
914 emphasis on the margins. *Chem. Geol.* 239, 156–164.  
915 <https://doi.org/10.1016/j.chemgeo.2006.11.013>

916 Jeandel, C., Oelkers, E.H., 2015. The influence of terrigenous particulate material dissolution on  
917 ocean chemistry and global element cycles. *Chem. Geol.* 395, 50–66.  
918 <https://doi.org/10.1016/j.chemgeo.2014.12.001>

919 Jelinek, A.R., Chemale, F., van der Beek, P.A., Guadagnin, F., Cupertino, J.A., Viana, A., 2014.  
920 Denudation history and landscape evolution of the northern East-Brazilian continental  
921 margin from apatite fission-track thermochronology. *J. South Am. Earth Sci.* 54, 158–  
922 181. <https://doi.org/10.1016/j.jsames.2014.06.001>

923 Kaminsky, F.V., Sablukov, S.M., Sablukova, L.I., Channer, D.M.DeR., 2004. Neoproterozoic  
924 ‘anomalous’ kimberlites of Guaniamo, Venezuela: Mica kimberlites of ‘isotopic  
925 transitional’ type. *Lithos, Selected Papers from the Eighth International Kimberlite  
926 Conference. Volume 1: The C. Roger Clement Volume 76*, 565–590.  
927 <https://doi.org/10.1016/j.lithos.2004.03.035>

928 Klaver, M., de Roever, E.W.F., Nanne, J.A.M., Mason, P.R.D., Davies, G.R., 2015.  
929 Charnockites and UHT metamorphism in the Bakhuis Granulite Belt, western Suriname:  
930 Evidence for two separate UHT events. *Precambrian Res.* 262, 1–19.  
931 <https://doi.org/10.1016/j.precamres.2015.02.014>

932 Kroonenberg, S.B., Roever, E.W.F. de, Fraga, L.M., Reis, N.J., Faraco, T., Lafon, J.-M.,  
933 Cordani, U., Wong, T.E., 2016. Paleoproterozoic evolution of the Guiana Shield in

934 Suriname: A revised model. *Neth. J. Geosci.* 95, 491–522.  
935 <https://doi.org/10.1017/njg.2016.10>

936 Larson, R.L., 1991. Latest pulse of Earth: Evidence for a mid-Cretaceous superplume. *Geology*  
937 19, 547–550. [https://doi.org/10.1130/0091-7613\(1991\)019<0547:LPOEEF>2.3.CO;2](https://doi.org/10.1130/0091-7613(1991)019<0547:LPOEEF>2.3.CO;2)

938 Lawrence, R.L., Cox, R., Mapes, R.W., Coleman, D.S., 2011. Hydrodynamic fractionation of  
939 zircon age populations. *GSA Bull.* 123, 295–305. <https://doi.org/10.1130/B30151.1>

940 Leal, A.B.M., Girardi, V. a. V., Leal, L.R.B., 2012. GEOLOGIA, PETROGRAFIA E  
941 GEOQUÍMICA DOS SILLS COTINGO E PEDRA PRETA, ESTADO DE RORAIMA,  
942 BRASIL. *Geochim. Bras.* 20, 233–250. <https://doi.org/10.21715/gb.v20i3.247>

943 Lenharo, S.L.R., Moura, M.A., Botelho, N.F., 2002. Petrogenetic and mineralization processes in  
944 Paleo- to Mesoproterozoic rapakivi granites: examples from Pitinga and Goiás, Brazil.  
945 *Precambrian Res.* 119, 277–299. [https://doi.org/10.1016/S0301-9268\(02\)00126-2](https://doi.org/10.1016/S0301-9268(02)00126-2)

946 Loewen, M.W., Duncan, R.A., Kent, A.J.R., Krawl, K., 2013. Prolonged plume volcanism in the  
947 Caribbean Large Igneous Province: New insights from Curaçao and Haiti. *Geochem.*  
948 *Geophys. Geosystems* 14, 4241–4259. <https://doi.org/10.1002/ggge.20273>

949 Loncke, L., Roest, W.R., Klingelhoefer, F., Basile, C., Graindorge, D., Heuret, A., Marcaillou,  
950 B., Museur, T., Fanget, A.S., Mercier de Lépinay, M., 2019. Transform marginal  
951 plateaus. *Earth-Sci. Rev.* 102940. <https://doi.org/10.1016/j.earscirev.2019.102940>

952 Louterbach, M., Roddaz, M., Antoine, P.-O., Marivaux, L., Adnet, S., Bailleul, J., Dantas, E.,  
953 Santos, R.V., Chemale, F., Baby, P., Sanchez, C., Calderon, Y., 2018. Provenance record  
954 of late Maastrichtian–late Palaeocene Andean Mountain building in the Amazonian  
955 retroarc foreland basin (Madre de Dios basin, Peru). *Terra Nova* 30, 17–23.  
956 <https://doi.org/10.1111/ter.12303>

957 MacRae, N.D., Nesbitt, H.W., Kronberg, B.I., 1992. Development of a positive Eu anomaly  
958 during diagenesis. *Earth Planet. Sci. Lett.* 109, 585–591. [https://doi.org/10.1016/0012-](https://doi.org/10.1016/0012-821X(92)90116-D)  
959 [821X\(92\)90116-D](https://doi.org/10.1016/0012-821X(92)90116-D)

960 Malusà, M.G., Carter, A., Limoncelli, M., Villa, I.M., Garzanti, E., 2013. Bias in detrital zircon  
961 geochronology and thermochronometry. *Chem. Geol.* 359, 90–107.  
962 <https://doi.org/10.1016/j.chemgeo.2013.09.016>

963 Malusà, M.G., Resentini, A., Garzanti, E., 2016. Hydraulic sorting and mineral fertility bias in  
964 detrital geochronology. *Gondwana Res.* 31, 1–19.  
965 <https://doi.org/10.1016/j.gr.2015.09.002>

966 Mann, P., Taylor, F.W., Edwards, R.L., Ku, T.-L., 1995. Actively evolving microplate formation  
967 by oblique collision and sideways motion along strike-slip faults: An example from the  
968 northeastern Caribbean plate margin. *Tectonophysics* 246, 1–69.  
969 [https://doi.org/10.1016/0040-1951\(94\)00268-E](https://doi.org/10.1016/0040-1951(94)00268-E)

970 Marques, S.N. de S., Souza, V. da S., Dantas, E.L., Valério, C. da S., Nascimento, R.S.C. do,  
971 2014. Contribuições para a petrografia, geoquímica e geocronologia (U-Pb e Sm-Nd) das  
972 rochas efusivas Paleoproterozóicas do Grupo Iricoumé, craton Amazônico, Brasil. *Braz.*  
973 *J. Geol.* 44, 121–138. <https://doi.org/10.5327/Z2317-4889201400010010>

974 Martin, E.E., Blair, S.W., Kamenov, G.D., Scher, H.D., Bourbon, E., Basak, C., Newkirk, D.N.,  
975 2010. Extraction of Nd isotopes from bulk deep sea sediments for paleoceanographic  
976 studies on Cenozoic time scales. *Chem. Geol.* 269, 414–431.  
977 <https://doi.org/10.1016/j.chemgeo.2009.10.016>

978 Martin, E.E., MacLeod, K.G., Jiménez Berrocoso, A., Bourbon, E., 2012. Water mass circulation  
979 on Demerara Rise during the Late Cretaceous based on Nd isotopes. *Earth Planet. Sci.*  
980 *Lett.* 327–328, 111–120. <https://doi.org/10.1016/j.epsl.2012.01.037>

981 Marzoli, A., Renne, P.R., Piccirillo, E.M., Ernesto, M., Bellieni, G., Min, A.D., 1999. Extensive  
982 200-Million-Year-Old Continental Flood Basalts of the Central Atlantic Magmatic  
983 Province. *Science* 284, 616–618. <https://doi.org/10.1126/science.284.5414.616>

984 Mascle, J., Blarez, E., 1987. Evidence for transform margin evolution from the Ivory Coast–  
985 Ghana continental margin. *Nature* 326, 378–381. <https://doi.org/10.1038/326378a0>

986 McLennan, S.M., 1989. Rare earth elements in sedimentary rocks; influence of provenance and  
987 sedimentary processes. *Rev. Mineral. Geochem.* 21, 169–200.

988 McLennan, S.M., Hemming, S., McDaniel, D.K., Hanson, G.N., 1993a. Geochemical approaches  
989 to sedimentation, provenance, and tectonics, in: *Geological Society of America Special*  
990 *Papers*. Geological Society of America, pp. 21–40. <https://doi.org/10.1130/SPE284-p21>

991 McLennan, S.M., Hemming, S., McDaniel, D.K., Hanson, G.N., 1993b. Geochemical  
992 approaches to sedimentation, provenance, and tectonics. *Geol. Soc. Am. Spec. Pap.* 284,  
993 21–40. <https://doi.org/10.1130/SPE284-p21>

994 McReath, I., Faraco, M.T.L., 2005. Paleoproterozoic greenstone-granite belts in Northern Brazil  
995 and the former Guyana Shield - West African Craton province. *Geol. USP Sér. Científica*  
996 5, 49–63. <https://doi.org/10.5327/S1519-874X2006000100004>

997 Mercier de Lépinay, M., Loncke, L., Basile, C., Roest, W.R., Patriat, M., Maillard, A., De  
998 Clarens, P., 2016. Transform continental margins – Part 2: A worldwide review.  
999 *Tectonophysics* 693, 96–115. <https://doi.org/10.1016/j.tecto.2016.05.038>

1000 Meyers, P.A., 1997. Organic geochemical proxies of paleoceanographic, paleolimnologic, and  
1001 paleoclimatic processes. *Org. Geochem.* 27, 213–250. <https://doi.org/10.1016/S0146->  
1002 6380(97)00049-1

1003 Meyers, P.A., Bernasconi, S.M., Forster, A., 2006. Origins and accumulation of organic matter  
1004 in expanded Albian to Santonian black shale sequences on the Demerara Rise, South  
1005 American margin. *Org. Geochem., Advances in Organic Geochemistry 2005* 37, 1816–  
1006 1830. <https://doi.org/10.1016/j.orggeochem.2006.08.009>

1007 Min, A.D., Piccirillo, E.M., Marzoli, A., Bellieni, G., Renne, P.R., Ernesto, M., Marques, L.S.,  
1008 2013. The Central Atlantic Magmatic Province (CAMP) in Brazil: Petrology,  
1009 Geochemistry,  $^{40}\text{Ar}/^{39}\text{Ar}$  Ages, Paleomagnetism and Geodynamic Implications, in: The  
1010 Central Atlantic Magmatic Province: Insights from Fragments of Pangea. American  
1011 Geophysical Union (AGU), pp. 91–128. <https://doi.org/10.1029/136GM06>

1012 Moiroud, M., Pucéat, E., Donnadiou, Y., Bayon, G., Guiraud, M., Voigt, S., Deconinck, J.-F.,  
1013 Monna, F., 2016. Evolution of neodymium isotopic signature of seawater during the Late  
1014 Cretaceous: Implications for intermediate and deep circulation. *Gondwana Res.* 36, 503–  
1015 522. <https://doi.org/10.1016/j.gr.2015.08.005>

1016 Monteiro, H.S., Vasconcelos, P.M.P., Farley, K.A., Lopes, C.A.M., 2018. Age and evolution of  
1017 diachronous erosion surfaces in the Amazon: Combining (U-Th)/He and cosmogenic  $^3\text{He}$   
1018 records. *Geochim. Cosmochim. Acta* 229, 162–183.  
1019 <https://doi.org/10.1016/j.gca.2018.02.045>

1020 Montgomery, C.W., Hurley, P.M., 1978. Total-rock UPb and RbSr systematics in the Imataca  
1021 Series, Guayana Shield, Venezuela. *Earth Planet. Sci. Lett.* 39, 281–290.  
1022 [https://doi.org/10.1016/0012-821X\(78\)90204-2](https://doi.org/10.1016/0012-821X(78)90204-2)

1023 Moquet, J.-S., Morera, S., Turcq, B., Poitrasson, F., Roddaz, M., Moreira-Turcq, P., Espinoza,  
1024 J.C., Guyot, J.-L., Takahashi, K., Orrillo-Vigo, J., Petrick, S., Mounic, S., Sondag, F.,  
1025 2020. Control of seasonal and inter-annual rainfall distribution on the Strontium-  
1026 Neodymium isotopic compositions of suspended particulate matter and implications for  
1027 tracing ENSO events in the Pacific coast (Tumbes basin, Peru). *Glob. Planet. Change*  
1028 185, 103080. <https://doi.org/10.1016/j.gloplacha.2019.103080>

1029 Morais Neto, J.M., Hegarty, K.A., Karner, G.D., Alkmim, F.F., 2009. Timing and mechanisms  
1030 for the generation and modification of the anomalous topography of the Borborema  
1031 Province, northeastern Brazil. *Mar. Pet. Geol.* 26, 1070–1086.  
1032 <https://doi.org/10.1016/j.marpetgeo.2008.07.002>

1033 Moreau, C., Ohnenstetter, D., Demaiffe, D., Robineau, B., 1996. The Los Archipelago nepheline  
1034 syenite ring-structure: A magmatic marker of the evolution of the central and equatorial  
1035 atlantic. *Can. Mineral.* 34, 281–299.

1036 Moulin, M., Aslanian, D., Unternehr, P., 2010. A new starting point for the South and Equatorial  
1037 Atlantic Ocean. *Earth-Sci. Rev.* 98, 1–37. <https://doi.org/10.1016/j.earscirev.2009.08.001>

1038 Murlot, Y., 2018. Contrôles sur la répartition des argiles organiques dans les bassins profonds :  
1039 cas de l'Atlantique central au Crétacé (thesis). <http://www.theses.fr>. Toulouse 3.

1040 Murlot, Y., Roddaz, M., Dera, G., Calvès, G., Kim, J., Chaboureau, A., Mounic, S., Raison, F.,  
1041 2018a. Geochemical Evidence for Large- Scale Drainage Reorganization in Northwest  
1042 Africa During the Cretaceous. *Geochem. Geophys. Geosystems* 0.  
1043 <https://doi.org/10.1029/2018GC007448>

1044 Murlot, Y., Calvès, G., Clift, P.D., Baby, G., Chaboureau, A.-C., Raison, F., 2018b. Seismic  
1045 stratigraphy of Cretaceous eastern Central Atlantic Ocean: Basin evolution and

1046 palaeoceanographic implications. *Earth Planet. Sci. Lett.* 499, 107–121.  
1047 <https://doi.org/10.1016/j.epsl.2018.07.023>

1048 Müller, R.D., Smith, W.H.F., 1993. Deformation of the oceanic crust between the North  
1049 American and South American Plates. *J. Geophys. Res. Solid Earth* 98, 8275–8291.  
1050 <https://doi.org/10.1029/92JB02863>

1051 Nemčok, M., Rybár, S., Sinha, S.T., Hermeston, S.A., Ledvényiová, L., 2016. Transform  
1052 margins: development, controls and petroleum systems – an introduction. *Geol. Soc.  
1053 Lond. Spec. Publ.* 431, 1–38. <https://doi.org/10.1144/SP431.15>

1054 Nesbitt, H.W., Young, G.M., 1982. Early Proterozoic climates and plate motions inferred from  
1055 major element chemistry of lutites. *Nature* 299, 715–717.  
1056 <https://doi.org/10.1038/299715a0>

1057 Nesbitt, H.W., Young, G.M., McLennan, S.M., Keays, R.R., 1996. Effects of Chemical  
1058 Weathering and Sorting on the Petrogenesis of Siliciclastic Sediments, with Implications  
1059 for Provenance Studies. *J. Geol.* 104, 525–542. <https://doi.org/10.1086/629850>

1060 Nixon, P.H., Davies, G.R., Rex, D.C., Gray, A., 1992. Venezuela kimberlites. *J. Volcanol.  
1061 Geotherm. Res.* 50, 101–115. [https://doi.org/10.1016/0377-0273\(92\)90039-G](https://doi.org/10.1016/0377-0273(92)90039-G)

1062 Nogueira, S.A.A., Bettencourt, J.S., Tassinari, C.C.G., 2017. GEOCHRONOLOGY OF THE  
1063 GRANITOID HOSTED SALAMANGONE GOLD DEPOSIT, LOURENÇO  
1064 DISTRICT, AMAPÁ, BRAZIL. *Rev. Bras. Geociências* 30, 261–264.

1065 Oliveira, E.C., Lafon, J.-M., Gioia, S.M.C.L., Pimentel, M.M., 2008. Datação Sm-Nd em rocha  
1066 total e granada do metamorfismo granulítico da região de Tartarugal Grande, Amapá  
1067 Central. *Rev. Bras. Geociências* 38, 114–127.

1068 Olszewski, W.J., Wirth, K.R., Gibbs, A.K., Gaudette, H.E., 1989. The age, origin, and tectonics  
1069 of the Grão Pará Group and associated rocks, Serra dos Carajás, Brazil: Archean  
1070 continental volcanism and rifting. *Precambrian Res.*, *Precambrian Research Recent*  
1071 *Advances of the Precambrian Geology of South and Central America and the Caribbean*  
1072 42, 229–254. [https://doi.org/10.1016/0301-9268\(89\)90013-2](https://doi.org/10.1016/0301-9268(89)90013-2)

1073 Olyphant, J.R., Johnson, R.A., Hughes, A.N., 2017. Evolution of the Southern Guinea Plateau:  
1074 Implications on Guinea-Demerara Plateau formation using insights from seismic,  
1075 subsidence, and gravity data. *Tectonophysics* 717, 358–371.  
1076 <https://doi.org/10.1016/j.tecto.2017.08.036>

1077 Othman, D.B., Polvé, M., Allègre, C.J., 1984. Nd—Sr isotopic composition of granulites and  
1078 constraints on the evolution of the lower continental crust. *Nature* 307, 510–515.  
1079 <https://doi.org/10.1038/307510a0>

1080 Palmer, M.R., Edmond, J.M., 1992. Controls over the strontium isotope composition of river  
1081 water. *Geochim. Cosmochim. Acta* 56, 2099–2111. [https://doi.org/10.1016/0016-](https://doi.org/10.1016/0016-7037(92)90332-D)  
1082 [7037\(92\)90332-D](https://doi.org/10.1016/0016-7037(92)90332-D)

1083 Patchett, P.J., Ross, G.M., Gleason, J.D., 1999. Continental Drainage in North America During  
1084 the Phanerozoic from Nd Isotopes. *Science* 283, 671–673.  
1085 <https://doi.org/10.1126/science.283.5402.671>

1086 Peulvast, J.-P., Bétard, F., 2015. A history of basin inversion, scarp retreat and shallow  
1087 denudation: The Araripe basin as a keystone for understanding long-term landscape  
1088 evolution in NE Brazil. *Geomorphology, Patterns and rates of Cenozoic landscape*  
1089 *change in orogenic and post-orogenic settings* 233, 20–40.  
1090 <https://doi.org/10.1016/j.geomorph.2014.10.009>

1091 Pindell, J.L., 1991. Geologic Rationale for Hydrocarbon Exploration in the Caribbean and  
1092 Adjacent Regions. *J. Pet. Geol.* 14, 237–258. <https://doi.org/10.1111/j.1747->  
1093 [5457.1991.tb00310.x](https://doi.org/10.1111/j.1747-5457.1991.tb00310.x)

1094 Posadas, V.G., Kalliokoski, J., 1967. Rb-Sr ages of the encrucijada granite intrusive in the  
1095 Imataca Complex, Venezuela. *Earth Planet. Sci. Lett.* 2, 210–214.  
1096 [https://doi.org/10.1016/0012-821X\(67\)90130-6](https://doi.org/10.1016/0012-821X(67)90130-6)

1097 Potter, P.E., 1997. The Mesozoic and Cenozoic paleodrainage of South America: a natural  
1098 history. *J. South Am. Earth Sci.* 10, 331–344. <https://doi.org/10.1016/S0895->  
1099 [9811\(97\)00031-X](https://doi.org/10.1016/S0895-9811(97)00031-X)

1100 Pourmand, A., Dauphas, N., Ireland, T.J., 2012. A novel extraction chromatography and MC-  
1101 ICP-MS technique for rapid analysis of REE, Sc and Y: Revising CI-chondrite and Post-  
1102 Archean Australian Shale (PAAS) abundances. *Chem. Geol.* 291, 38–54.  
1103 <https://doi.org/10.1016/j.chemgeo.2011.08.011>

1104 Priem, H.N.A., Boelrijk, N. a. I.M., Hebeda, E.H., Verdurmen, E. a. T., Verschure, R.H., 1971.  
1105 Isotopic Ages of the Trans-Amazonian Acidic Magmatism and the Nickerie Metamorphic  
1106 Episode in the Precambrian Basement of Suriname, South America. *GSA Bull.* 82, 1667–  
1107 1680. [https://doi.org/10.1130/0016-7606\(1971\)82\[1667:IAOTTA\]2.0.CO;2](https://doi.org/10.1130/0016-7606(1971)82[1667:IAOTTA]2.0.CO;2)

1108 Priem, H.N.A., Boelrijk, N. a. I.M., Hebeda, E.H., Verdurmen, E.A.T., Verschure, R.H., 1973.  
1109 Age of the Precambrian Roraima Formation in Northeastern South America: Evidence  
1110 from Isotopic Dating of Roraima Pyroclastic Volcanic Rocks in Suriname. *GSA Bull.* 84,  
1111 1677–1684. [https://doi.org/10.1130/0016-7606\(1973\)84<1677:AOTPRF>2.0.CO;2](https://doi.org/10.1130/0016-7606(1973)84<1677:AOTPRF>2.0.CO;2)

1112 Reis, N.J., Teixeira, W., Hamilton, M.A., Bispo-Santos, F., Almeida, M.E., D’Agrella-Filho,  
1113 M.S., 2013. Avanavero mafic magmatism, a late Paleoproterozoic LIP in the Guiana

1114 Shield, Amazonian Craton: U–Pb ID-TIMS baddeleyite, geochemical and paleomagnetic  
1115 evidence. *Lithos, Large Igneous Provinces (LIPs) and Supercontinents* 174, 175–195.  
1116 <https://doi.org/10.1016/j.lithos.2012.10.014>

1117 Reuber, K.R., Pindell, J., Horn, B.W., 2016. Demerara Rise, offshore Suriname: Magma-rich  
1118 segment of the Central Atlantic Ocean, and conjugate to the Bahamas hot spot.  
1119 *Interpretation* 4, T141–T155. <https://doi.org/10.1190/INT-2014-0246.1>

1120 Roddaz, M., Nauton-Fourteu, M., Santos, R.V., Dantas, E.L., Calves, G., 2020. Controls on the  
1121 provenance of late Eocene to Quaternary Mozambique Channel shales (DSDP 25 Site  
1122 242). *Mar. Geol.* 421, 106090. <https://doi.org/10.1016/j.margeo.2019.106090>

1123 Roddaz, M., Viers, J., Brusset, S., Baby, P., Boucayrand, C., Hérail, G., 2006. Controls on  
1124 weathering and provenance in the Amazonian foreland basin: Insights from major and  
1125 trace element geochemistry of Neogene Amazonian sediments. *Chem. Geol.* 226, 31–65.  
1126 <https://doi.org/10.1016/j.chemgeo.2005.08.010>

1127 Roddaz, M., Viers, J., Brusset, S., Baby, P., Hérail, G., 2005. Sediment provenances and  
1128 drainage evolution of the Neogene Amazonian foreland basin. *Earth Planet. Sci. Lett.*  
1129 239, 57–78. <https://doi.org/10.1016/j.epsl.2005.08.007>

1130 Roddaz, M., Viers, J., Moreira-Turcq, P., Blondel, C., Sondag, F., Guyot, J.-L., Moreira, L.,  
1131 2014. Evidence for the control of the geochemistry of Amazonian floodplain sediments  
1132 by stratification of suspended sediments in the Amazon. *Chem. Geol.* 387, 101–110.  
1133 <https://doi.org/10.1016/j.chemgeo.2014.07.022>

1134 Rousseau, T.C.C., Roddaz, M., Moquet, J.-S., Delgado, H.H., Calves, G., Bayon, G., 2019.  
1135 Controls on the geochemistry of suspended sediments from large tropical South

1136 American rivers (Amazon, Orinoco and Maroni). *Chem. Geol.*  
1137 <https://doi.org/10.1016/j.chemgeo.2019.05.027>

1138 Rousseau, T.C.C., Sonke, J.E., Chmeleff, J., Beek, P. van, Souhaut, M., Boaventura, G., Seyler,  
1139 P., Jeandel, C., 2015. Rapid neodymium release to marine waters from lithogenic  
1140 sediments in the Amazon estuary. *Nat. Commun.* 6, 1–8.  
1141 <https://doi.org/10.1038/ncomms8592>

1142 Santos, J.O.S., Hartmann, L.A., Gaudette, H.E., Groves, D.I., Mcnaughton, N.J., Fletcher, I.R.,  
1143 2000. A New Understanding of the Provinces of the Amazon Craton Based on Integration  
1144 of Field Mapping and U-Pb and Sm-Nd Geochronology. *Gondwana Res.* 3, 453–488.  
1145 [https://doi.org/10.1016/S1342-937X\(05\)70755-3](https://doi.org/10.1016/S1342-937X(05)70755-3)

1146 Santos, R.V., Sondag, F., Cochonneau, G., Lagane, C., Brunet, P., Hattingh, K., Chaves, J.G.S.,  
1147 2015. Source area and seasonal  $^{87}\text{Sr}/^{86}\text{Sr}$  variations in rivers of the Amazon basin.  
1148 *Hydrol. Process.* 29, 187–197. <https://doi.org/10.1002/hyp.10131>

1149 Sapin, F., Davaux, M., Dall’asta, M., Lahmi, M., Baudot, G., Ringenbach, J.-C., 2016. Post-rift  
1150 subsidence of the French Guiana hyper-oblique margin: from rift-inherited subsidence to  
1151 Amazon deposition effect. *Geol. Soc. Lond. Spec. Publ.* 431, 125–144.  
1152 <https://doi.org/10.1144/SP431.11>

1153 Sato, K., 1998. *Evolução Crustal da Plataforma Sul Americana, com Base na Geoquímica*  
1154 *Isotópica Sm-Nd (text).* Universidade de São Paulo.  
1155 <https://doi.org/10.11606/T.44.1998.tde-29102012-144139>

1156 Schlanger, S.O., Jenkyns, H.C., 1976. Cretaceous Oceanic Anoxic Events: Causes and  
1157 Consequences. *Geol. En Mijnb.* 55.

1158 Schulte, P., Deutsch, A., Salge, T., Berndt, J., Kontny, A., MacLeod, K.G., Neuser, R.D.,  
1159 Krumm, S., 2009. A dual-layer Chicxulub ejecta sequence with shocked carbonates from  
1160 the Cretaceous–Paleogene (K–Pg) boundary, Demerara Rise, western Atlantic. *Geochim.*  
1161 *Cosmochim. Acta* 73, 1180–1204. <https://doi.org/10.1016/j.gca.2008.11.011>

1162 Sibuet, J.-C., Mascle, J., 1978. Plate kinematic implications of Atlantic equatorial fracture zone  
1163 trends. *J. Geophys. Res. Solid Earth* 83, 3401–3421.  
1164 <https://doi.org/10.1029/JB083iB07p03401>

1165 Souza, V. da S., Souza, A.G.H. de, Dantas, E.L., Valério, C. da S., Souza, V. da S., Souza,  
1166 A.G.H. de, Dantas, E.L., Valério, C. da S., 2015. K’Mudku A-type magmatism in the  
1167 southernmost Guyana Shield, central-north Amazon Craton (Brazil): the case of Pedra do  
1168 Gavião syenogranite. *Braz. J. Geol.* 45, 293–306.  
1169 <https://doi.org/10.1590/23174889201500020008>

1170 Spooner, C.M., Berrangé, J.P., Fairbairn, H.W., 1971. Rb-Sr Whole-Rock Age of the Kanuku  
1171 Complex, Guyana. *GSA Bull.* 82, 207–210. [https://doi.org/10.1130/0016-](https://doi.org/10.1130/0016-7606(1971)82[207:RWAOTK]2.0.CO;2)  
1172 [7606\(1971\)82\[207:RWAOTK\]2.0.CO;2](https://doi.org/10.1130/0016-7606(1971)82[207:RWAOTK]2.0.CO;2)

1173 Tassinari, C.C.G., 1981. Evolução geotectônica da província Rio Negro-Jurena na região  
1174 amazônica (text). Universidade de São Paulo. [https://doi.org/10.11606/D.44.1981.tde-](https://doi.org/10.11606/D.44.1981.tde-11062013-163626)  
1175 [11062013-163626](https://doi.org/10.11606/D.44.1981.tde-11062013-163626)

1176 Tassinari, C.C.G., Munhá, J.M.U., Teixeira, W., Palácios, T., Nutman, A.P., S, C.S., Santos,  
1177 A.P., Calado, and B.O., 2004. The Imataca Complex, NW Amazonian Craton,  
1178 Venezuela: Crustal evolution and integration of geochronological and petrological  
1179 cooling histories. *Episodes J. Int. Geosci.* 27, 3–12.  
1180 <https://doi.org/10.18814/epiiugs/2004/v27i1/002>

1181 Taylor, S.R., McLennan, S.M., 1985. The continental crust: Its composition and evolution.

1182 Teixeira, W., Tassinari, C.C.G., Cordani, U.G., Kawashita, K., 1989. A review of the  
1183 geochronology of the Amazonian Craton: Tectonic implications. *Precambrian Res.*,  
1184 *Precambrian Research Recent Advances of the Precambrian Geology of South and*  
1185 *Central America and the Caribbean* 42, 213–227. [https://doi.org/10.1016/0301-](https://doi.org/10.1016/0301-9268(89)90012-0)  
1186 [9268\(89\)90012-0](https://doi.org/10.1016/0301-9268(89)90012-0)

1187 Tello Saenz, C.A., Hackspacher, P.C., Hadler Neto, J.C., Iunes, P.J., Guedes, S., Ribeiro, L.F.B.,  
1188 Paulo, S.R., 2003. Recognition of Cretaceous, Paleocene, and Neogene tectonic  
1189 reactivation through apatite fission-track analysis in Precambrian areas of southeast  
1190 Brazil: association with the opening of the south Atlantic Ocean. *J. South Am. Earth Sci.*  
1191 15, 765–774. [https://doi.org/10.1016/S0895-9811\(02\)00131-1](https://doi.org/10.1016/S0895-9811(02)00131-1)

1192 Torsvik, T.H., Van der Voo, R., Preeden, U., Mac Niocaill, C., Steinberger, B., Doubrovine,  
1193 P.V., van Hinsbergen, D.J.J., Domeier, M., Gaina, C., Tohver, E., Meert, J.G.,  
1194 McCausland, P.J.A., Cocks, L.R.M., 2012. Phanerozoic polar wander, palaeogeography  
1195 and dynamics. *Earth-Sci. Rev.* 114, 325–368.  
1196 <https://doi.org/10.1016/j.earscirev.2012.06.007>

1197 Tyson, R., 1995. *Sedimentary Organic Matter: Organic facies and palynofacies*. Springer  
1198 Netherlands. <https://doi.org/10.1007/978-94-011-0739-6>

1199 Vanderhaeghe, O., Ledru, P., Thiéblemont, D., Egal, E., Cocherie, A., Tegye, M., Milési, J.-P.,  
1200 1998. Contrasting mechanism of crustal growth: Geodynamic evolution of the  
1201 Paleoproterozoic granite–greenstone belts of French Guiana. *Precambrian Res.* 92, 165–  
1202 193. [https://doi.org/10.1016/S0301-9268\(98\)00074-6](https://doi.org/10.1016/S0301-9268(98)00074-6)

- 1203 Vermeesch, P., 2018. Statistical models for point-counting data. *Earth Planet. Sci. Lett.* 501,  
1204 112–118. <https://doi.org/10.1016/j.epsl.2018.08.019>
- 1205 Vermeesch, P., 2004. How many grains are needed for a provenance study? *Earth Planet. Sci.*  
1206 *Lett.* 224, 441–451. <https://doi.org/10.1016/j.epsl.2004.05.037>
- 1207 Viers, J., Roddaz, M., Filizola, N., Guyot, J.-L., Sondag, F., Brunet, P., Zouiten, C., Boucayrand,  
1208 C., Martin, F., Boaventura, G.R., 2008. Seasonal and provenance controls on Nd–Sr  
1209 isotopic compositions of Amazon rivers suspended sediments and implications for Nd  
1210 and Sr fluxes exported to the Atlantic Ocean. *Earth Planet. Sci. Lett.* 274, 511–523.  
1211 <https://doi.org/10.1016/j.epsl.2008.08.011>
- 1212 Voicu, G., Bardoux, M., Stevenson, R., Jébrak, M., 2000. Nd and Sr isotope study of  
1213 hydrothermal scheelite and host rocks at Omai, Guiana Shield: implications for ore fluid  
1214 source and flow path during the formation of orogenic gold deposits. *Miner. Deposita* 35,  
1215 302–314. <https://doi.org/10.1007/s001260050243>
- 1216 Weltje, G.J., 2012. Quantitative models of sediment generation and provenance: State of the art  
1217 and future developments. *Sediment. Geol., Actualistic Models of Sediment Generation*  
1218 280, 4–20. <https://doi.org/10.1016/j.sedgeo.2012.03.010>
- 1219 White, W.M., Dupré, B., Vidal, P., 1985. Isotope and trace element geochemistry of sediments  
1220 from the Barbados Ridge-Demerara Plain region, Atlantic Ocean. *Geochim. Cosmochim.*  
1221 *Acta* 49, 1875–1886. [https://doi.org/10.1016/0016-7037\(85\)90082-1](https://doi.org/10.1016/0016-7037(85)90082-1)
- 1222 Yang, W., Escalona, A., 2011. Tectonostratigraphic evolution of the Guyana Basin. *AAPG Bull.*  
1223 95, 1339–1368. <https://doi.org/10.1306/01031110106>

1224

1225 **Figure captions**

1226 **Figure 1.** A) Location of study area in its Cretaceous paleogeographical context (Torsvik et al.,  
1227 2012). The red rectangle indicates position of area shown on Figure 1B. WAC: West African  
1228 Craton. B) Map of the Precambrian Guiana Shield, Mesozoic Takutu basin (TkB), and location  
1229 of studied Arapaima-1 well (AR-1, red circle)

1230 **Figure 2.** Stratigraphy and sedimentary log section of Arapaima-1 well including  $\delta^{13}\text{C}_{\text{TOC}}$  data,  
1231 TOC contents, sedimentation rate and main geodynamic events at the scale of Guyana-Suriname  
1232 basin. The stratigraphic position of analyzed samples is indicated by orange triangle. AR-1:  
1233 Arapaima-1 well. M: mudstone. W: wackestone. P: packstone. G: grainstone. C: clay. S: silt. FS:  
1234 fine sandstone. MS: medium sandstone. CS: coarse sandstone. Details on the calculation of  
1235 sedimentation rates can be found in (Mourlot, 2018). References for timing and duration of main  
1236 geodynamic events are as follow : South Atlantic Ocean opening (Hall et al., 2018), Equatorial  
1237 Atlantic Ocean opening (Moulin et al., 2010; Sibuet and Mascle, 1978), Albian-Coniacian  
1238 cooling (Benkhelil et al., 1995; Yang and Escalona, 2011), Central Atlantic spreading rate  
1239 acceleration (Larson, 1991), Caribbean Large Igneous Province (Loewen et al., 2013), Andean  
1240 deformation (Hurtado et al., 2018; Louterbach et al., 2018).

1241 **Figure 3.** Map showing the main geological units of the Guiana Shield (simplified from  
1242 (Kroonenberg et al., 2016)) and the localization of the main northern South American rivers.  
1243 Mean values for  $\varepsilon_{\text{Nd}(0)}$  and  $^{87}\text{Sr}/^{86}\text{Sr}$  isotopic composition of the main geological unit of the  
1244 Guiana Shield are given (See Table 1 and text for details and references).

1245 **Figure 4.** Major and selected trace element contents of analyzed samples normalized to PAAS  
1246 (Pourmand et al., 2012; Taylor and McLennan, 1985). From left to right on the diagram, these

1247 include the major elements (SiO<sub>2</sub>, TiO<sub>2</sub>, Al<sub>2</sub>O<sub>3</sub>, Fe<sub>2</sub>O<sub>3</sub>, MnO, MgO, CaO, Na<sub>2</sub>O, K<sub>2</sub>O and P<sub>2</sub>O<sub>5</sub>),  
1248 LILE (Rb, Cs, Ba, Sr, Th and U), HFSE (Y, Zr, Nb, Hf), and TTE (Sc, Cr, Co, V and Ni).

1249 **Figure 5.** Rare earth element (REE) contents of studied samples normalized to PAAS (Pourmand  
1250 et al., 2012; Taylor and McLennan, 1985).

1251 **Figure 6.** Stratigraphic variation of Nd and Sr isotope compositions (expressed as  $\epsilon_{Nd(0)}$  and  
1252  $^{87}Sr/^{86}Sr$ ) and selected trace element ratios (Cr/Th, Th/Sc and Eu/Eu\*, see text for details) of  
1253 analyzed samples. The lengths of the horizontal bar for the Sr-Nd isotopic compositions  
1254 correspond to 1 $\sigma$  analytical errors (see Table 4). The horizontal bars for the Cr/Th, Th/Sc, and  
1255 Eu/Eu\* ratios correspond to 15% (i.e., the sum of the Cr and Th concentration analytical errors),  
1256 25% (i.e., the sum of the Th and Sc concentration analytical errors) and 5% (i.e., the Eu  
1257 concentration analytical error, see supplementary material Table S2). Dashed lines in Eu/Eu\*,  
1258 Th/Sc and Cr/Th show the PAAS ratio values (Taylor and McLennan, 1985; Pourmand et al.,  
1259 2012). Red and blue rectangles indicate the values range for felsic and basic sediments,  
1260 respectively (Cullers, 2000).

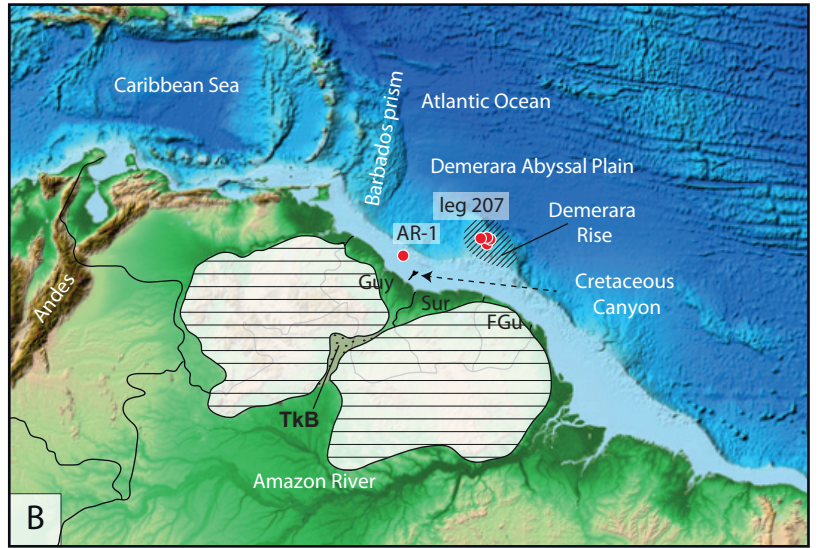
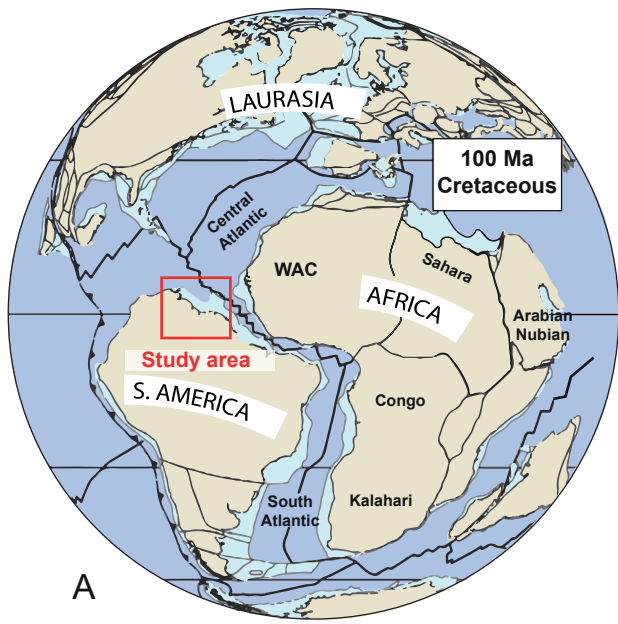
1261 **Figure 7.** HREE/LREE vs. MREE/MREE\* diagram. HREE/LREE and MREE/MREE\* values  
1262 are calculated following (Martin et al., 2010) where HREE=Tm+Yb+Lu, LREE=La+Pr+Nd,  
1263 MREE=Gd+Tb+Dy (all PAAS normalized), and MREE\*=the average of HREE+LREE. The  
1264 MREE bulge and “bell-shaped” REE profiles correspond to REE patterns observed in fish teeth,  
1265 Fe-Mn oxides, organic matter and pore waters, while “HREE-enriched” profiles correspond to  
1266 modern sea water (Huck et al., 2016; Moiroud et al., 2016). These end-members reflect the REE  
1267 contents of marine sediments influenced by seawater or authigenic phases, while “flat” REE

1268 patterns are characteristic of continental clays (see Huck et al., 2016; Moiroud et al., 2016 for a  
1269 review). Analyzed samples are represented by specific symbols used in Figs 4 and 5.

1270 **Figure 8.** Cross-plots of  $\varepsilon_{\text{Nd}(0)}$  and  $^{87}\text{Sr}/^{86}\text{Sr}$  values for the analyzed samples. The isotopic fields  
1271 of potential end-members of the Guiana Shield are based on a compilation of published data (see  
1272 Table 1 and supporting Table S1). AAIG: Archean granitoids (AAIG) (Barreto et al., 2013; da  
1273 Rosa-Costa et al., 2006; Hurley et al., 1968; Montgomery and Hurley, 1978; Oliveira et al.,  
1274 2008; Olszewski et al., 1989; Othman et al., 1984; Posadas and Kalliokoski, 1967; Tassinari et  
1275 al., 2004) (Avelar et al. (2003); PGGF: Paleoproterozoic granitoids and felsic series (Barreto et  
1276 al., 2013; Boher et al., 1992; da Rosa-Costa et al., 2006; Gaudette et al., 1978; Gruau et al., 1985;  
1277 Hurley et al., 1968; Lenharo et al., 2002; Marques et al., 2014; McReath and Faraco, 2005;  
1278 Nogueira et al., 2000; Priem et al., 1973, 1971; Sato, 1998; Tassinari, 1981; Voicu et al., 2000),  
1279 Macambira et al. (1987) Jorge Joao et al. (1985), Gibbs and Barron (1993 Avelar et al. (2003);  
1280 PHGB: Paleoproterozoic high-grade belt (Gaudette et al., 1996; Heinonen et al., 2012; Klaver et  
1281 al., 2015; Othman et al., 1984; Sato, 1998; Spooner et al., 1971; Tassinari, 1981) de Roever et al.  
1282 (2003) ; MG : Mesoproterozoic granitoids (Heinonen et al., 2012; Souza et al., 2015; Tassinari,  
1283 1981); PMI-GB: Paleoproterozoic mafic intrusions and greenstone belt (Gibbs et al., 1986;  
1284 Gruau et al., 1985; Hebeda et al., 1973; Kaminsky et al., 2004; Leal et al., 2006; McReath and  
1285 Faraco, 2005; Nixon et al., 1992; Santos et al., 2000; Sato, 1998; Voicu et al., 2000); JMD:  
1286 Jurassic mafic dykes (Deckart et al., 2005; Min et al., 2013). To avoid outlier effects and  
1287 important overlapping, the limits of each rectangular field are defined as the first quartile and the  
1288 third quartile for each subset. Comparative clay data from the Demerara Rise and Demerara  
1289 abyssal plain are added (Martin et al., 2012; Schulte et al., 2009; White et al., 1985). Sr-Nd  
1290 isotopic compositions of suspended particulate matter and dissolved Sr transported by the main

1291 tropical rivers of the northeastern part of South America (i.e., Amazon, lower and upper Orinoco,  
1292 Rio Negro, Maroni, Trombetas, Caroni) (Allègre et al., 1996; Goldstein et al., 1997; Palmer and  
1293 Edmond, 1992; Rousseau et al., 2019; Santos et al., 2015) are added. Note that, when unavailable,  
1294 sediment  $^{87}\text{Sr}/^{86}\text{Sr}$  values of rivers were replaced by water  $^{87}\text{Sr}/^{86}\text{Sr}$  values.

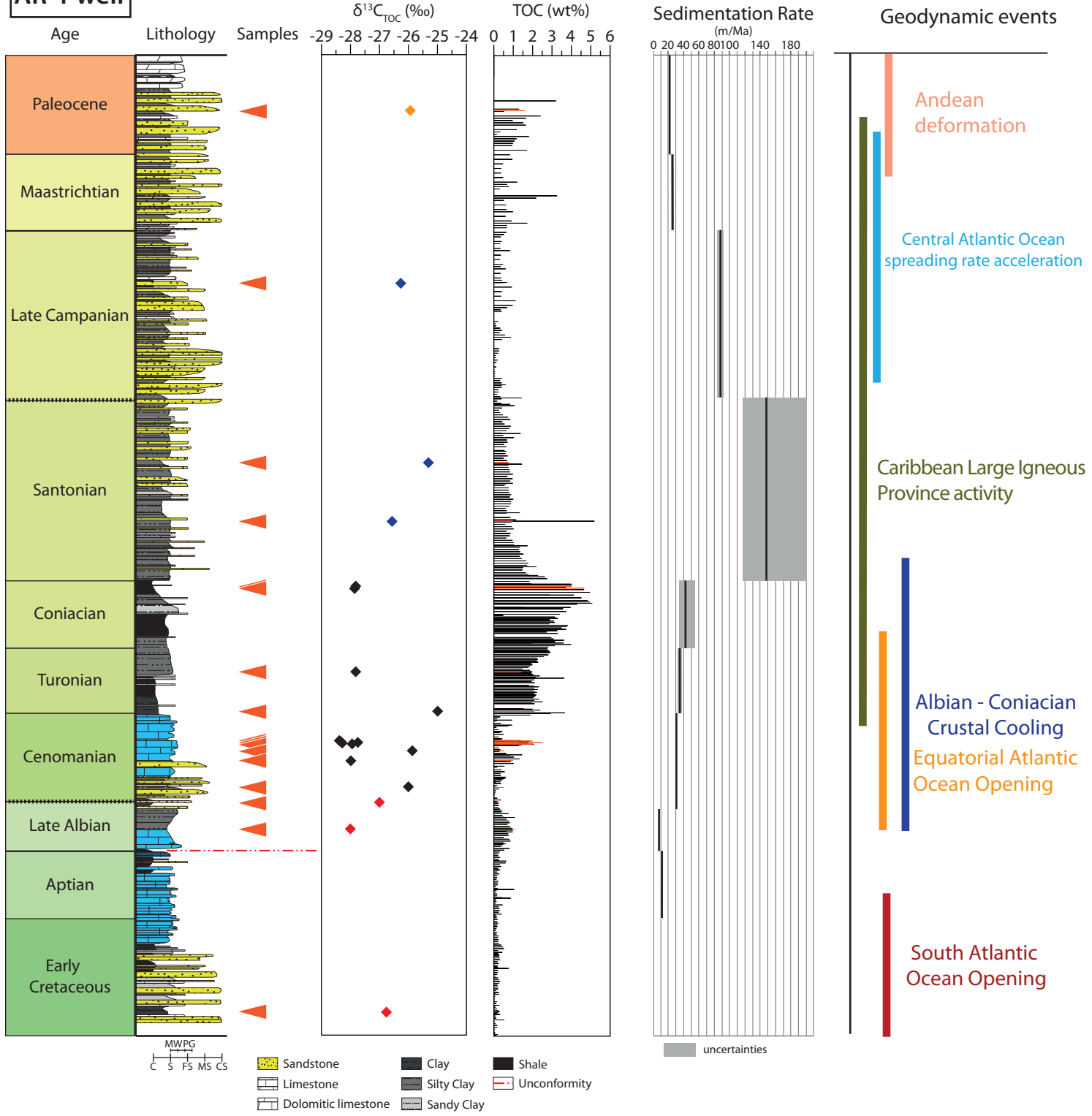
1295 **Figure 9.** Paleogeographic map at 90 Ma (modified from Scotese and Golonka (1997) showing  
1296 potential provenance areas for the Guyana-Suriname basin for pre-Coniacian (in red dashed  
1297 curve) and post-Coniacian (blue dashed curve) times. TkB: Takutu basin. AR-1: Arapaima-1  
1298 well.

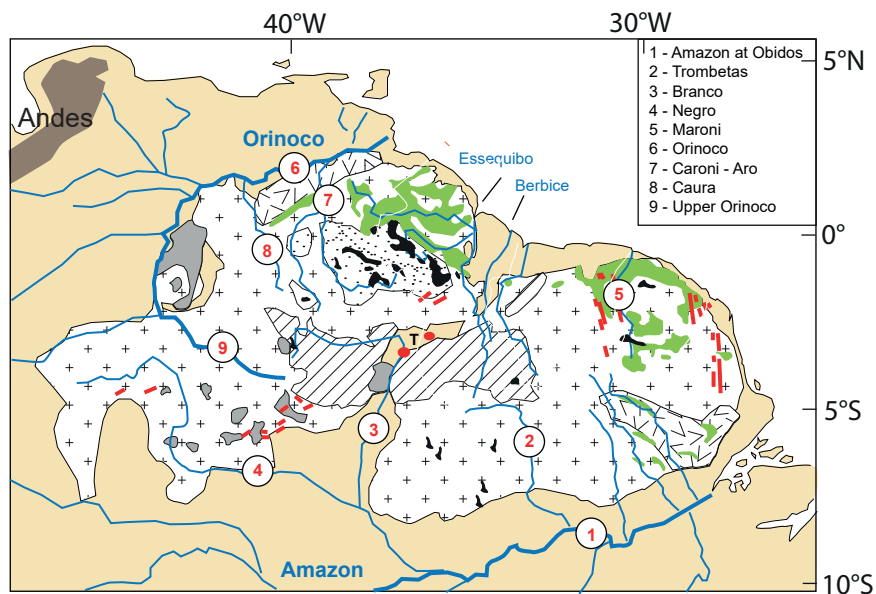


- Continent
- Shallow marine
- Deep marine

- Precambrian Guiana Shield
- Mesozoic sedimentary basin

# AR-1 well



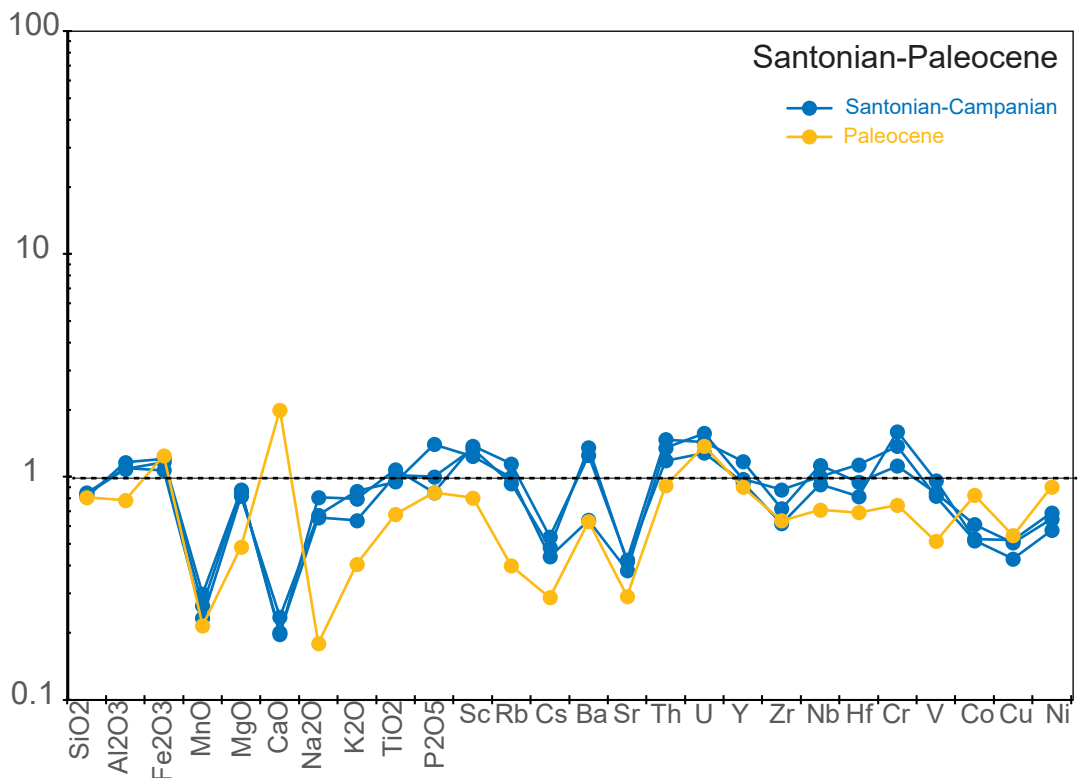
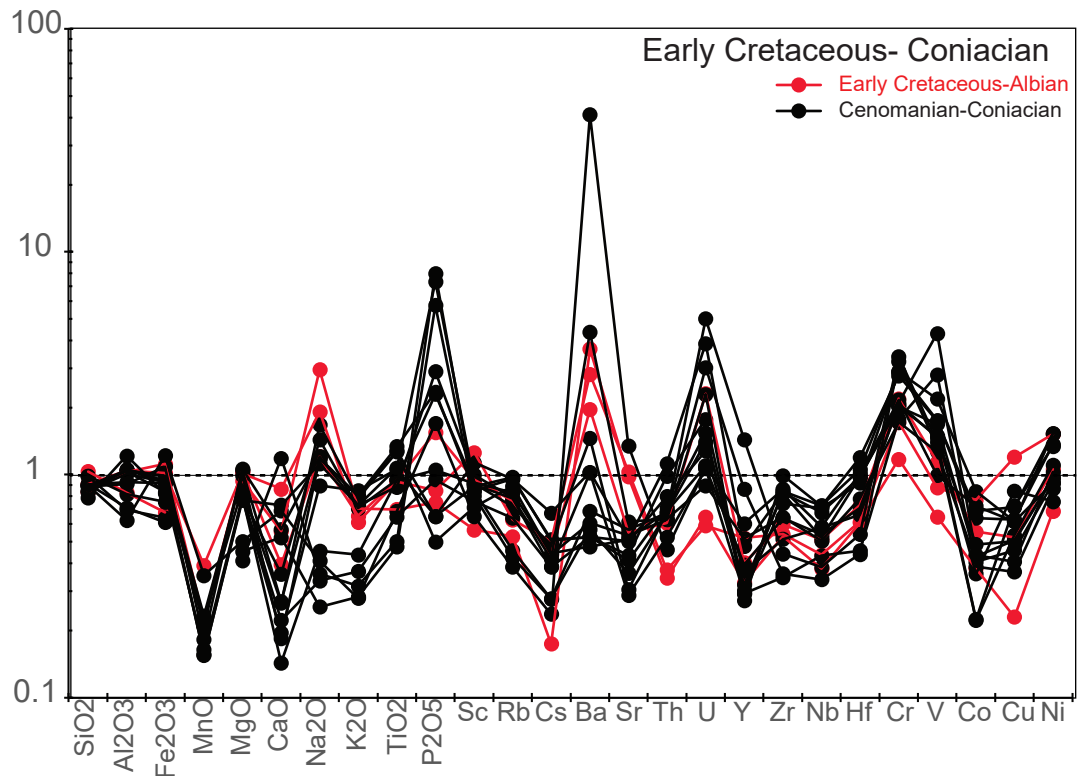


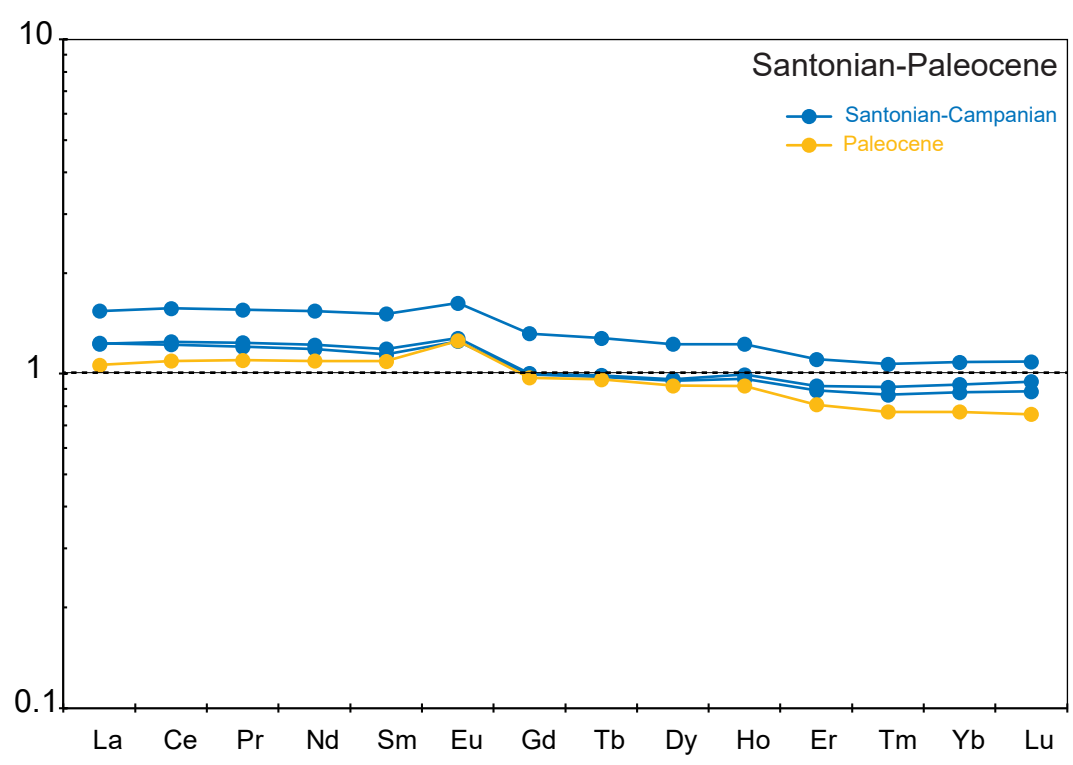
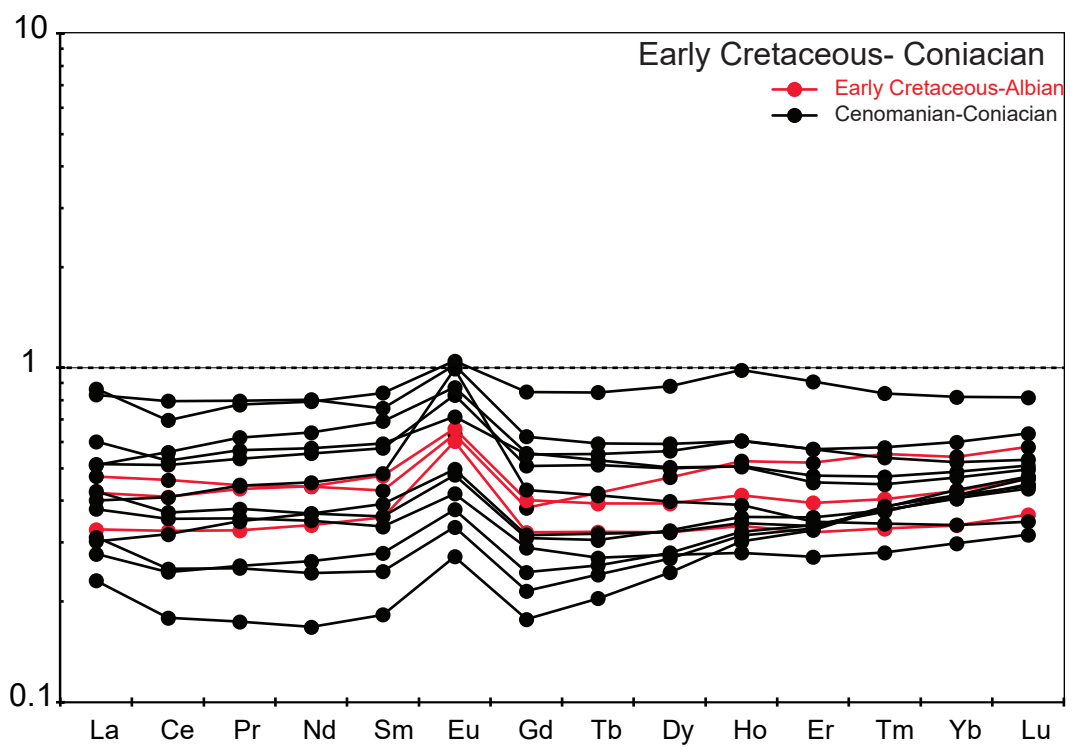
**Felsic to intermediate sources:**

- 
 AAIG - Archean Amapa & Imataca granitoids  
 ( $\epsilon_{Nd}(0)=-31.4$   $^{87}Sr/^{86}Sr=0.79509$ )
- 
 PGGF - Paleoproterozoic granitoids, gneiss & felsic volcanism  
 ( $\epsilon_{Nd}(0)=-23.4$   $^{87}Sr/^{86}Sr=0.77395$ )
- 
 PHGB - Paleoproterozoic high-grade granulite belts  
 ( $\epsilon_{Nd}(0)=-21.2$   $^{87}Sr/^{86}Sr=0.72025$ )
- 
 PRS - Paleoproterozoic Roraima sandstones
- 
 MG - Mesoproterozoic granites  
 ( $\epsilon_{Nd}(0)=-18.5$   $^{87}Sr/^{86}Sr=0.77460$ )

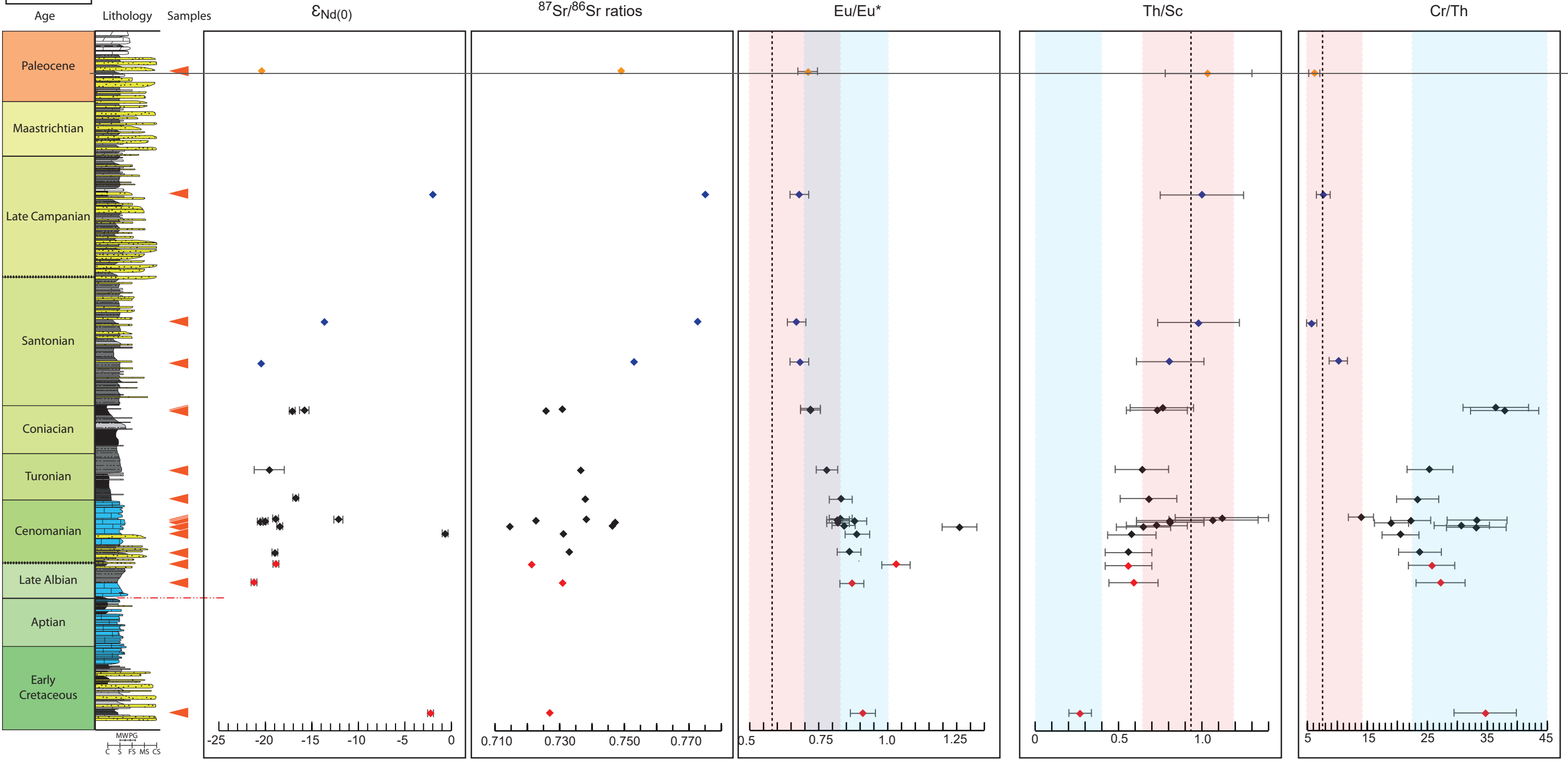
**Mafic to ultramafic sources:**

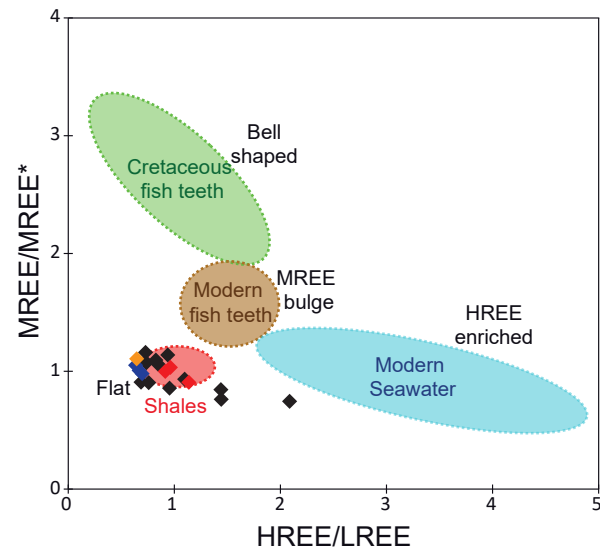
- 
 GB - Greenstone Belt (metavolcanic)  
 ( $\epsilon_{Nd}(0)=-8.9$   $^{87}Sr/^{86}Sr=0.71051$ )
- 
 PMI - Precambrian mafic intrusions  
 ( $\epsilon_{Nd}(0)=-8.9$   $^{87}Sr/^{86}Sr=0.71051$ )
- 
 JMD - Jurassic mafic dykes  
 ( $\epsilon_{Nd}(0)=-0.2$   $^{87}Sr/^{86}Sr=0.70647$ )
- 
 Phanerozoic sedimentary cover

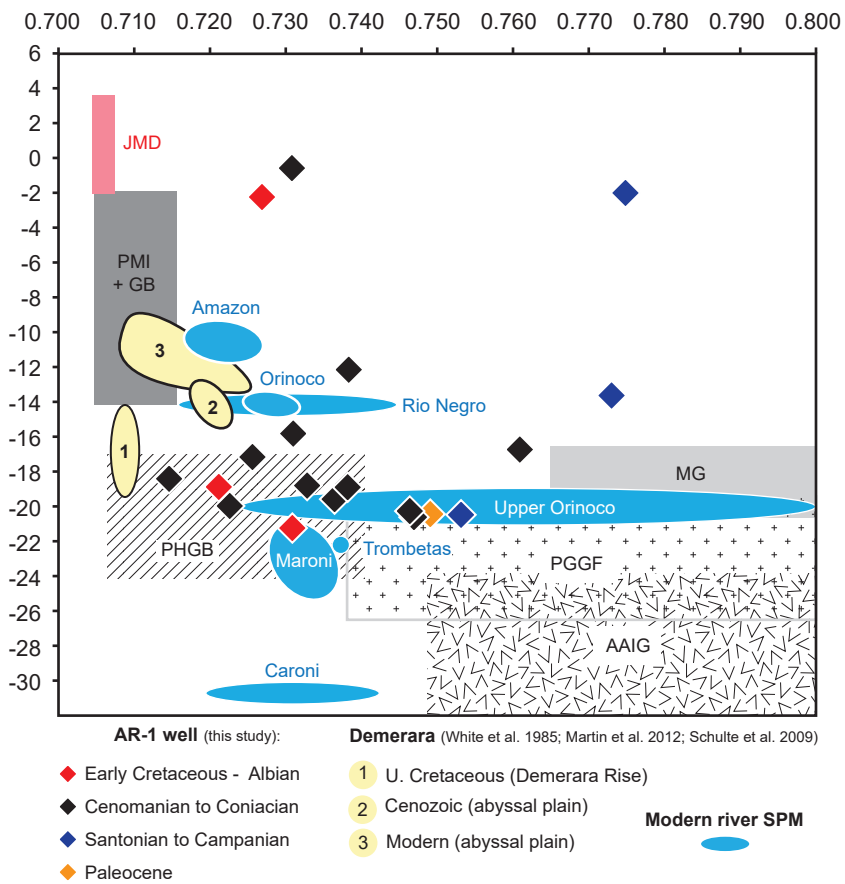


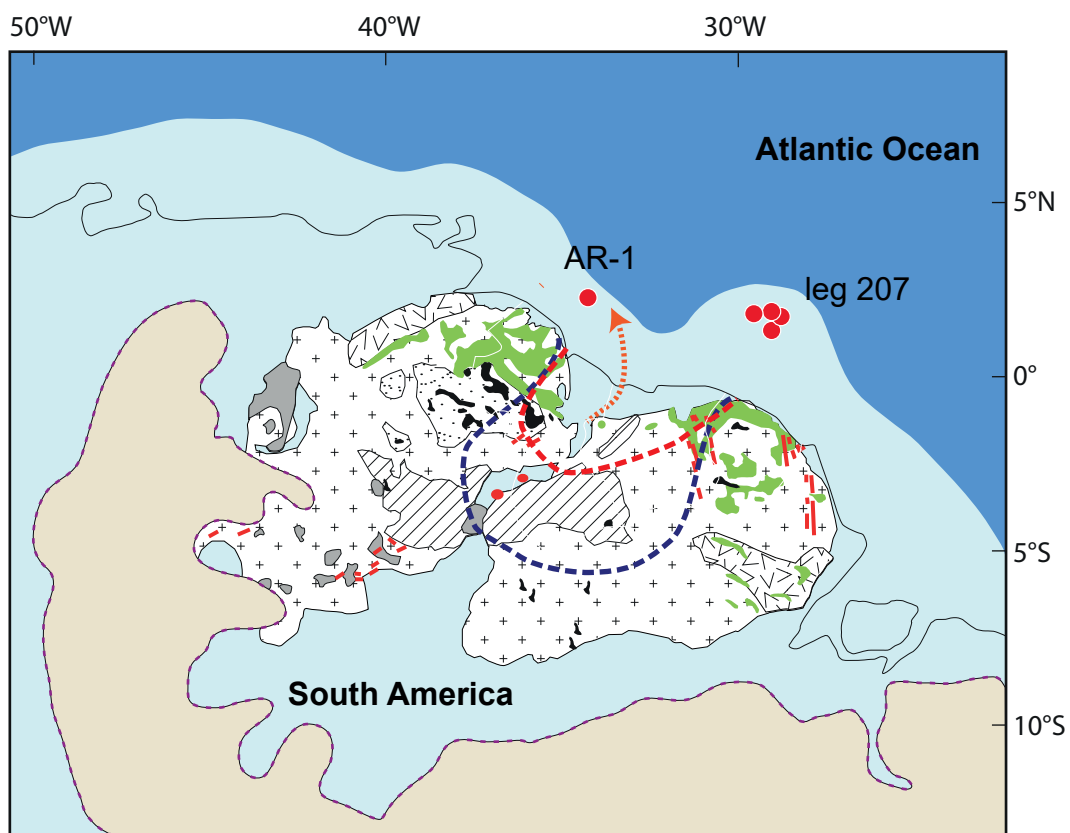


AR1 well









### Paleogeography

- Shallow marine
- Deep ocean
- Continent
- Coast Line
- Pre Coniacian Catchment areas
- Post Coniacian Catchment areas
- Sedimentary Supply

### Source Ages

#### Felsic to intermediate sources:

- AAIG - Archean Amapa & Imataca granitoids
- PGGF - Paleoproterozoic granitoids, gneiss & felsic volcanism
- PHGB - Paleoproterozoic high-grade granulite belts
- PRS - Paleoproterozoic Roraima sandstones
- MG - Mesoproterozoic granites

#### Mafic to ultramafic sources:

- GB - Greenstone Belt (metavolcanic)
- PMI - Precambrian mafic intrusions
- JMD - Jurassic mafic dykes
- Phanerozoic sedimentary cover

$\epsilon_{Nd(0)}$	AAIG	PGGF	PMI+GB	MG	PHGB	JMD
N	59	93	32	8	31	43
Min	-42.8	-42.8	-19.3	-21.2	-36.4	-4.6
Max	-1.9	-11.4	4.1	-15.3	-2.1	5.7
Mean	-30.2	-23.9	-7.8	-18.3	-20.4	0.4
Std. error	1.2	0.6	1.2	0.8	1.4	0.5
Variance	86.5	38.2	49.9	4.5	64.5	9.4
Stand. dev	9.3	6.2	7.1	2.1	8.0	3.1
Median	-31.4	-23.4	-8.9	-18.5	-21.2	-0.2
25 prcntil	-37.1	-26.6	-14.2	-20.5	-24.1	-2.1
75 prcntil	-23.9	-19.5	-1.9	-16.5	-17.1	3.6

$^{87}Sr/^{86}Sr$	AAIG	PGGF	PMI+GB	MG	PHGB	JMD
N	52	214	26	5	40	51
Min	0.70857	0.7015	0.704448	0.7645	0.7012	0.70292
Max	2.7365	4.4008	0.72945	0.8804	1.58175	0.711148
Mean	0.8880397	0.9097801	0.7111302	0.80524	0.7598767	0.706221
Std. error	0.0465425	0.0317048	0.0013489	0.023468	0.0248467	0.000237
Variance	0.1126428	0.2151119	4.73E-05	0.0027537	0.0246944	2.87E-06
Stand. dev	0.335623	0.4638016	0.0068782	0.0524761	0.1571444	0.0016928
Median	0.795095	0.77395	0.71051	0.7746	0.72025	0.70647
25 prcntil	0.7489525	0.738245	0.7048952	0.76535	0.7065225	0.70462
75 prcntil	0.838575	0.875025	0.7157525	0.86045	0.7402675	0.70746

**Table 1:** Mean  $\epsilon_{Nd(0)}$  values and  $^{87}Sr/^{86}Sr$  isotopic composition and statistical parameters for potential end members; N: number of samples analyzed

Std error: Standard error; Stand. Dev: Standard deviation; 25 prcntil: first quartile; 75 prcntil: third quartile;

AAIG: Archean granitoid ; PGGF: Paleoproterozoic granitoids and felsic series; PMI+GB: Paleoproterozoic mafic intrusions and greenstone belt;

PHGB: Paleoproterozoic high-grade belt; MG: Mesoproterozoic granitoids; JMD: Jurassic Mafic Dykes

Data references:

AAIG: Barreto et al., 2013; da Rosa-Costa et al., 2006; Hurley et al., 1968; Montgomery and Hurley, 1978; Oliveira et al., 2008; Olszewski et al., 1989; Othman et al., 1984; Posadas and Kalliokoski, 1967; Tassinari et al., 2004) (Avelar et al. (2003); PGGF: Paleoproterozoic granitoids and felsic series (Barreto et al., 2013; Boher et al., 1992; da Rosa-Costa et al., 2006; Gaudette et al., 1978; Gruau et al., 1985; Hurley et al., 1968; Lenharo et al., 2002; Marques et al., 2014; McReath and Faraco, 2005; Nogueira et al., 2000; Priem et al., 1973, 1971; Sato, 1998; Tassinari, 1981; Voicu et al., 2000), Macambira et al. (1987) Jorge Joao et al. (1985), Gibbs and Barron (1993 Avelar et al. (2003); PHGB: Paleoproterozoic high-grade belt (Gaudette et al., 1996; Heinonen et al., 2012; Klaver et al., 2015; Othman et al., 1984; Sato, 1998; Spooner et al., 1971; Tassinari, 1981) de Roever et al. (2003) ; MG : Mesoproterozoic granitoids (Heinonen et al., 2012; Souza et al., 2015; Tassinari, 1981); PMI-GB: Paleoproterozoic mafic intrusions and greenstone belt (Gibbs et al., 1986; Gruau et al., 1985; Hebeda et al., 1973; Kaminsky et al., 2004; Leal et al., 2006; McReath and Faraco, 2005; Nixon et al., 1992; Santos et al., 2000; Sato, 1998; Voicu et al., 2000); JMD: Jurassic mafic dykes (Deckart et al., 2005; De Min et al., 2003)

Sample	Age	$\delta^{13}\text{C}_{\text{TOC}}$ (‰ VPDB)	TOC (wt%)
AR1-1	Early Cretaceous	-26.7	0.2
AR1-6	Aptian	-28.0	1.1
AR1-7	Late Albian	-27.0	0.3
AR1-8	Late Albian	-26.1	0.5
AR1-9	Cenomanian	-28.0	1.0
AR1-10	Cenomanian	-25.8	0.5
AR1-11B	Cenomanian	-27.9	2.0
AR1-11C	Cenomanian	-28.3	1.3
AR1-11D	Cenomanian	-27.7	2.5
AR1-11E	Cenomanian	-28.4	1.9
AR1-11F	Cenomanian	-28.4	1.4
AR1-12A	Early Turonian	-25.0	2.1
AR1-14	Turonian	-27.9	1.6
AR1-17A	Coniacian	-28.0	4.6
AR1-17B	Coniacian	-27.8	4.0
AR1-20	Late Santonian	-26.6	1.0
AR1-21	Santonian?	-25.4	0.7
AR1-23	Late Campanian	-26.3	0.4
AR1-24	Paleocene	-25.9	1.6

**Table 2 :** Organic Matter Contents and Stable Carbon Isotope Values (TOC and  $\delta^{13}\text{C}_{\text{TOC}}$ ) of Sedimentary Rocks Analysed in this Study

Sample	AR1-1	AR1-6	AR1-7	AR1-8	AR1-9	AR1-10	AR1-11B	AR1-11C	AR1-11D
Age	Early Cretaceous	Late Albian	Late Albian	Cenomanian	Cenomanian	Cenomanian	Cenomanian	Cenomanian	Cenomanian
wt%									
SiO <sub>2</sub>	57.09	52.54	64.90	55.92	55.48	56.28	53.10	56.19	56.59
Al <sub>2</sub> O <sub>3</sub>	19.72	19.43	15.71	19.78	17.17	11.80	19.78	19.54	17.54
Fe <sub>2</sub> O <sub>3</sub>	6.60	7.25	4.40	6.05	7.06	7.92	6.43	5.44	5.94
MnO	0.04	0.02	< D.L.	0.02	0.02	0.04	0.02	0.02	0.02
MgO	2.23	2.28	2.06	1.72	2.34	1.11	2.18	1.74	1.91
CaO	1.12	0.52	0.73	0.25	0.74	0.90	0.24	0.47	0.35
Na <sub>2</sub> O	2.30	1.45	3.55	1.07	1.45	0.49	1.42	1.72	2.01
K <sub>2</sub> O	2.27	2.42	2.61	3.14	2.70	1.03	2.96	2.62	2.89
TiO <sub>2</sub>	0.93	0.94	0.70	1.06	0.88	0.69	1.28	0.95	1.27
P <sub>2</sub> O <sub>5</sub>	0.17	0.31	0.15	0.13	0.58	0.34	0.13	0.46	0.10
LOI	7.67	12.71	5.46	10.91	11.46	16.75	12.79	11.28	10.76
Total	100.13	99.86	100.27	100.04	99.86	97.34	100.33	100.42	99.37
Al/Si	0.39	0.42	0.27	0.4	0.35	0.24	0.42	0.39	0.35
CIA	70	77	61	78	72	77	77	75	71
ppm									
Sc	19.99	15.09	8.99	18.03	15.86	10.32	14.11	14.38	11.36
Rb	100.58	122.28	84.48	152.45	125.62	61.58	155.82	125.04	142.04
Cs	7.49	6.53	2.61	10.10	6.27	3.56	7.58	5.77	6.57
Ba	1836.12	1277.34	2383.46	666.73	2829.03	26793.14	342.00	341.76	394.32
Sr	206.01	109.76	195.54	103.58	123.21	269.75	82.50	100.41	106.65
Th	5.45	8.86	5.02	10.01	9.21	6.74	10.36	11.67	9.20
U	1.83	7.15	2.01	3.40	2.77	3.34	4.78	3.96	7.11
Y	14.2	11.0	9.0	16.5	14.1	10.8	8.0	8.8	7.4
Zr	113.51	125.81	111.17	180.52	135.19	134.04	155.75	172.29	208.16
Nb	8.31	9.68	7.19	11.07	9.59	10.24	13.45	9.91	13.72
Hf	3.08	3.65	3.04	5.06	3.90	3.53	4.59	4.88	5.96
Cr	188.87	241.18	129.11	237.96	189.08	223.43	318.57	222.02	306.20
V	131.11	170.71	96.99	149.10	189.91	224.00	328.04	253.35	261.33
Co	17.68	12.74	8.74	16.64	9.34	8.26	19.35	9.87	15.84
Cu	59.98	26.15	11.49	30.82	22.90	42.30	30.89	25.37	35.73
Ni	83.74	58.08	37.68	50.53	50.53	41.69	84.40	53.40	83.96
Zn	75.66	97.99	53.24	54.71	103.01	89.60	92.53	142.13	114.22
La	21.07	18.82	14.63	36.97	22.94	17.86	13.87	13.48	10.28
Ce	40.70	36.29	28.68	70.13	45.19	36.16	22.10	28.02	15.76
Pr	4.53	4.41	3.31	8.08	5.43	4.50	2.55	3.53	1.77
Nd	16.46	16.49	12.62	29.99	20.68	16.94	9.08	13.69	6.25
Sm	2.95	3.27	2.46	5.20	3.96	3.32	1.69	2.69	1.26
Eu	0.77	0.80	0.73	1.24	1.01	1.21	0.41	0.61	0.33
Gd	2.30	2.43	1.94	3.76	3.07	2.60	1.30	1.91	1.07
Tb	0.38	0.35	0.29	0.53	0.46	0.37	0.21	0.28	0.18
Dy	2.50	2.09	1.72	3.16	2.67	2.12	1.43	1.72	1.30
Ho	0.55	0.44	0.35	0.63	0.53	0.41	0.33	0.36	0.32
Er	1.60	1.21	0.99	1.76	1.46	1.07	1.02	1.03	1.01
Tm	0.25	0.18	0.15	0.26	0.21	0.15	0.17	0.17	0.17
Yb	1.63	1.29	1.02	1.80	1.47	1.02	1.25	1.22	1.30
Lu	0.26	0.21	0.16	0.28	0.22	0.15	0.21	0.20	0.21
Ta	0.88	0.96	2.32	1.52	0.98	0.94	1.31	0.97	1.34
Sm/Nd	0.18	0.20	0.19	0.17	0.19	0.20	0.19	0.20	0.20
Eu/Eu*	0.91	0.87	1.03	0.86	0.89	1.26	0.84	0.82	0.88
ΩCe	1.00	0.96	0.99	0.98	0.98	0.97	0.89	0.98	0.88
Cr/Th	34.6	27.2	25.7	23.8	20.5	33.2	30.8	19.0	33.3
Th/Sc	0.27	0.59	0.56	0.56	0.58	0.65	0.73	0.81	0.81
Zr/Sc	5.68	8.34	12.37	10.01	8.52	12.99	11.04	11.98	18.32
LREE	1.58	1.51	1.15	2.82	1.86	1.5	0.94	1.18	0.66
HREE	1.8	1.39	1.11	1.95	1.58	1.1	1.36	1.32	1.38
MREE	1.55	1.45	1.18	2.2	1.85	1.52	0.88	1.16	0.76
MREE*	1.69	1.45	1.13	2.38	1.72	1.3	1.15	1.25	1.02

Table 3: Major and Trace Element Concentrations of Sedimentary Rocks Analyzed in this Study . D.L. : Detection Limit

Note. Uncertainties for all elements are given in the supplementary material (Table S2)

LREE = La<sub>PAAS</sub> + Pr<sub>PAAS</sub> + Nd<sub>PAAS</sub> (in ppm); MREE = Gd<sub>PAAS</sub> + Tb<sub>PAAS</sub> + Dy<sub>PAAS</sub> (in ppm);

HREE = Tm<sub>PAAS</sub> + Yb<sub>PAAS</sub> + Lu<sub>PAAS</sub> (in ppm); MREE\* = (HREE+LREE) / 2;

CIA=[Al<sub>2</sub>O<sub>3</sub>/(Al<sub>2</sub>O<sub>3</sub>+CaO\*+Na<sub>2</sub>O+K<sub>2</sub>O)] ×100 (in molar proportions); Eu/Eu\* = Eu<sub>N</sub>/(Sm<sub>N</sub> × Gd<sub>N</sub>)<sup>1/2</sup>

where XN refers to the chondrite-normalized concentration value [Condie, 1993];

ΩCe = 2 × (Ce<sub>sample</sub>/Ce<sub>PAAS</sub>) / [(La<sub>sample</sub>/La<sub>PAAS</sub>) + (Pr<sub>sample</sub>/Pr<sub>PAAS</sub>)]

Sample	AR1-11E	AR1-11F	AR1-12A	AR1-14	AR1-17A	AR1-17B	AR1-20	AR1-21	AR1-23	AR1-24
Age	Cenomanian	Cenomanian	Early Turonian	Turonian	Coniacian	Coniacian	Early Santonian	Santonian?	Late Campanian	Paleocene
wt%										
SiO <sub>2</sub>	52.29	53.10	49.47	61.86	57.11	61.77	52.75	51.21	53.19	50.80
Al <sub>2</sub> O <sub>3</sub>	20.00	19.04	22.95	15.43	13.45	13.13	20.50	21.98	20.75	14.83
Fe <sub>2</sub> O <sub>3</sub>	6.10	6.01	5.35	4.91	3.98	4.16	7.57	7.83	6.96	8.09
MnO	0.02	0.02	< D.L.	< D.L.	< D.L.	< D.L.	0.03	0.03	0.02	0.02
MgO	2.30	1.69	1.76	1.78	0.91	1.00	1.89	1.92	1.80	1.07
CaO	0.35	0.95	0.19	0.29	1.54	0.68	0.26	0.26	0.31	2.60
Na <sub>2</sub> O	1.43	1.34	0.55	0.40	0.43	0.31	0.79	0.97	0.81	0.22
K <sub>2</sub> O	2.98	2.68	1.62	1.36	1.17	1.05	2.36	2.95	3.19	1.50
TiO <sub>2</sub>	1.34	1.07	0.95	0.65	0.50	0.47	1.02	1.08	0.95	0.68
P <sub>2</sub> O <sub>5</sub>	0.47	1.47	0.21	0.19	1.60	1.15	0.20	0.17	0.28	0.17
LOI	12.47	12.24	16.19	12.36	18.58	16.90	12.45	11.76	12.00	19.90
Total	99.75	99.60	99.22	99.23	99.26	100.62	99.80	100.16	100.26	99.87
Al/Si	0.43	0.41	0.53	0.28	0.27	0.24	0.44	0.49	0.44	0.33
CIA	76	74	89	85	74	82	83	81	80	69
ppm										
Sc	13.43	14.62	14.52	12.08	13.44	12.75	21.22	21.86	19.65	12.81
Rb	153.68	132.56	115.22	102.31	73.22	67.93	149.33	183.20	159.01	63.81
Cs	7.69	6.65	7.30	5.81	4.16	4.17	7.25	8.07	6.57	4.31
Ba	340.37	308.91	946.30	664.12	446.69	369.73	877.89	810.99	415.59	410.19
Sr	87.07	101.91	61.06	57.60	113.04	72.26	83.53	84.92	76.10	58.28
Th	14.39	16.37	9.87	7.68	9.84	9.72	17.25	21.49	19.67	13.35
U	5.49	12.01	4.35	3.30	15.54	9.38	3.97	4.44	4.86	4.27
Y	8.3	13.0	10.0	8.0	39.3	23.5	25.8	32.0	26.6	24.6
Zr	177.27	174.12	107.77	72.74	92.63	75.43	129.46	151.13	183.69	133.55
Nb	13.81	12.86	10.98	8.21	7.30	6.43	17.58	21.42	19.01	13.49
Hf	5.27	4.86	3.30	2.28	2.70	2.20	4.09	4.73	5.67	3.46
Cr	319.80	228.02	230.77	195.32	372.85	354.00	175.32	122.98	150.74	82.26
V	263.30	220.20	645.18	421.17	210.40	199.49	144.34	127.21	122.75	76.96
Co	14.68	11.18	10.03	8.88	5.16	5.12	12.10	14.05	11.89	19.01
Cu	31.50	25.16	20.33	18.32	36.12	26.80	26.05	25.31	21.44	27.25
Ni	75.29	53.16	56.40	47.64	73.86	60.67	37.91	35.60	31.67	49.59
Zn	106.40	80.21	68.22	67.48	114.85	98.88	79.63	74.47	69.55	53.10
La	12.36	22.79	19.02	16.84	38.51	26.80	54.96	68.63	54.75	47.31
Ce	21.60	49.30	32.55	31.18	61.50	46.51	107.93	138.54	109.94	96.33
Pr	2.59	6.28	3.84	3.60	7.87	5.75	12.22	15.76	12.56	11.14
Nd	9.85	23.89	13.67	13.03	29.58	21.46	44.25	57.53	45.55	40.74
Sm	1.92	4.76	2.47	2.30	5.79	4.08	7.86	10.39	8.15	7.50
Eu	0.46	1.07	0.58	0.51	1.28	0.87	1.53	1.98	1.56	1.53
Gd	1.48	3.35	1.87	1.75	5.11	3.32	6.00	7.96	6.06	5.87
Tb	0.23	0.47	0.27	0.24	0.75	0.49	0.87	1.14	0.88	0.86
Dy	1.49	2.69	1.74	1.47	4.70	3.00	5.07	6.54	5.14	4.91
Ho	0.34	0.53	0.38	0.29	1.03	0.64	1.01	1.29	1.04	0.97
Er	1.04	1.40	1.10	0.84	2.80	1.76	2.74	3.41	2.83	2.49
Tm	0.17	0.20	0.17	0.13	0.38	0.24	0.39	0.48	0.41	0.35
Yb	1.25	1.42	1.23	0.90	2.46	1.57	2.65	3.26	2.79	2.31
Lu	0.19	0.22	0.19	0.14	0.36	0.23	0.39	0.48	0.42	0.33
Ta	1.34	1.22	1.06	0.77	0.69	0.61	1.63	2.03	1.84	1.34
Sm/Nd	0.19	0.20	0.18	0.18	0.20	0.19	0.18	0.18	0.18	0.18
Eu/Eu*	0.83	0.82	0.83	0.78	0.72	0.72	0.68	0.67	0.68	0.71
ΩCe	0.92	0.99	0.92	0.96	0.85	0.90	1.00	1.01	1.01	1.01
Cr/Th	22.2	13.9	23.4	25.4	37.9	36.4	10.2	5.7	7.7	6.2
Th/Sc	1.07	1.12	0.68	0.64	0.73	0.76	0.81	0.98	1	1.04
Zr/Sc	13.2	11.91	7.42	6.02	6.89	5.92	6.1	6.91	9.35	10.43
LREE	0.92	2.05	1.36	1.26	2.82	2.02	4.2	5.38	4.28	3.77
HREE	1.32	1.52	1.3	0.96	2.66	1.71	2.83	3.48	2.99	2.47
MREE	0.95	1.93	1.15	1.02	3.13	2.03	3.56	4.66	3.6	3.48
MREE*	1.12	1.78	1.33	1.11	2.74	1.87	3.51	4.43	3.63	3.12

Table 2 (Continued)

Sample	Age	Sr (ppm)	$^{87}\text{Sr}/^{86}\text{Sr}$	$\pm 1\sigma$ ( $\times 10^6$ )	Nd (ppm)	$^{143}\text{Nd}/^{144}\text{Nd}$	$\pm 1\sigma$	$\epsilon_{\text{Nd}(0)}$	$\pm 1\sigma$	$T_{\text{DM}}$ (Ga)
AR1-1	Early Cretaceous	206.01	0.726863	0.000005	16.46	0.512523	0.000016	-2.2	0.3	0.9
AR1-6	Late Albian	109.76	0.730869	0.000005	16.49	0.511549	0.0000047	-21.2	0.1	2.6
AR1-7	Late Albian	195.54	0.721161	0.000003	12.62	0.51167	0.000008	-18.9	0.2	2.3
AR1-8	Cenomanian	103.58	0.732824	0.000003	29.99	0.511674	0.000008	-18.8	0.2	2.1
AR1-9	Cenomanian	123.21	0.730814	0.000005	20.68	0.512608	0.000011	-0.6	0.2	0.8
AR1-10	Cenomanian	269.75	0.714598	0.000005	16.94	0.511694	0.000004	-18.4	0.1	2.3
AR1-11B	Cenomanian	82.50	0.746371	0.000006	9.08	0.511599	0.000005	-20.3	0.1	2.3
AR1-11C	Cenomanian	100.41	0.746923	0.000005	13.69	0.511581	0.000006	-20.6	0.1	2.5
AR1-11D	Cenomanian	106.65	0.722602	0.000005	6.25	0.511614	0.000009	-20.0	0.2	2.5
AR1-11E	Cenomanian	87.07	0.738315	0.000005	9.85	0.512015	0.000025	-12.2	0.5	1.8
AR1-11F	Cenomanian	101.91	0.738174	0.000004	23.89	0.511669	0.000006	-18.9	0.1	2.4
AR1-12A	Early Turonian	61.06	0.760897	0.000005	13.67	0.51178	0.00001	-16.7	0.2	2.0
AR1-14	Turonian	57.60	0.736446	0.000005	13.03	0.511634	0.000083	-19.6	1.6	2.2
AR1-17A	Coniacian	113.04	0.725604	0.000005	29.58	0.5117585	0.000011	-17.2	0.2	2.2
AR1-17B	Coniacian	72.26	0.730986	0.000005	21.46	0.511827	0.000026	-15.8	0.5	2.0
AR1-20	Late Santonian	83.53	0.753144	0.000004	44.25	0.511588	0.000006	-20.5	0.1	2.2
AR1-21	Santonian ?	84.92	0.773011	0.000006	57.53	0.511939	0.000006	-13.6	0.1	1.8
AR1-23	Late Campanian	76.10	0.774847	0.000006	45.55	0.512535	0.000008	-2.0	0.2	0.9
AR1-24	Paleocene	58.275	0.749076	0.000005	40.74	0.51159	0.000003	-20.4	0.1	2.3

Table 4: Nd–Sr isotopic systematics of sedimentary rocks analyzed in this study